Impact of Bolt Pretension on Bearing Strength for All-Steel Members and Composite Members

JIA-HAU LIU and MICHEL BRUNEAU

ABSTRACT

Bolted connections are widely used in steel structures, and their design for slip-critical resistance and bearing strength is well documented in past research and current standards. However, the physical behavior that explains how friction and bearing forces interact in a pretensioned bolted connection and how these forces evolve under axial deformation remains unclear. This paper investigates the influence of bolt pretension on bearing strength through finite element analyses of both all-steel and composite splices [the latter one, of the type that would be found in composite plate shear walls/concrete filled (C-PSW/CF)]. The analyses captured the behavior of bolted connection, showing significant reduction in friction forces as bolt hole elongation increased. A simplified free-body diagram with contact springs was then employed to explain the yielding and bending of bolts, the loss of clamping forces, and the thinning of plates (due to the Poisson ratio effect), all of which contribute to the reduction of friction as hole elongation increases. Additionally, the study examines how bolt pretension affects C-PSW/CF connections under compression, showing that concrete restricts hole deformation and allows friction forces to be sustained until the concrete cracks and deformation progresses.

Keywords: bolted connections, bolt pretension, composite plate shear wall/concrete filled, finite element analysis.

INTRODUCTION AND BACKGROUND

Bolted connections are widely used in steel structures due to their efficiency and ease of construction. The design of these connections is sometimes governed by two main limit states: slip-critical resistance and bearing strength. Since the plies in a bearing connection are required to be in firm contact, pretension may be applied in a bearing connection, not only in slip-critical connections, but also in bearing-type connections. The application of pretension induces friction between the bolts and steel plates, which complicates the understanding of how friction and bearing stresses contribute to the overall strength of the connection. Previous studies have investigated bearing-type bolted connections, contributing to the development of bearing strength parameters as outlined in current standards (Brown et al., 2007; Frank and Yura, 1981; Kim and Yura, 1996; Kulak et al., 1987; Lewis and Zwememan, 1996). According to the AISC *Specification for Structural Steel Buildings* (AISC, 2022b), hereafter referred to as the AISC *Specification*, the calculations for bearing strength and slip-critical resistance of a bolted connection are considered separately.

To compare the effect of bolt clamping forces, Frank and Yura (1981) conducted a series of tests for specimens with fully tensioned and not fully tensioned bolts for the bearing and net section failure type connections. The findings indicated that fully tensioned bolts exhibit a 10% higher capacity compared to snug-tightened bolts when failure is defined as the point when hole deformation is equal to 0.25 in. Note that the pretension in snug-tight bolts is not reported in these studies and that there is no upper limit on the pretension in a snug-tight bolt (although, technically, it should be low). However, no increase in capacity was observed when failure is defined in terms of ultimate load for the bearing-controlled connections. Kulak et al. (1987) compared earlier bearing test results from studies by Back and Bouwman (1959), Frank and Yura (1981), Hirano (1970), Jones (1958), and Nunse (1959). The test results indicated that the application of a clamping force somewhat increased the “ultimate bearing strength,” suggesting partial load transmission through friction. Note that the “ultimate bearing strength” here refers to the failure loads observed during testing. Consequently, the “actual bearing strength” (i.e., the portion of the total bearing strength that is due to the contact stresses acting on a bolt hole) is lower than the “ultimate bearing strength” calculated based on the total applied load.

More recently, Može (2018) conducted a series of bearing tests on bolted connections with large end distances and bolt spacings and used finite element analysis to investigate the development of friction force during axial tensile

---

Jia-Hau Liu, Graduate Research Assistant, Department of Civil Structural and Environmental Engineering, University at Buffalo, Buffalo, N.Y. ORCID: https://orcid.org/0009-0003-9608-1932. Email: jiahauli@buffalo.edu (corresponding)

Michel Bruneau, SUNY Distinguished Professor, Department of Civil Structural and Environmental Engineering, University at Buffalo, Buffalo, N.Y. ORCID: http://orcid.org/0000-0003-1170-468X. Email: bruneau@buffalo.edu

Paper No. 2024-14

ISSN 2997-4720

loading of several single-bolt connections. The analyses also included a preloaded connection with a friction coefficient of 0.15 for comparison. Results from this latter analysis demonstrated that friction forces are generated between contact interfaces during axial loading, even without bolt pretension, and that these forces increase when the friction coefficient is greater. The friction forces in the preloaded connections showed no significant difference compared to those without preload once large deformations are developed. These analysis results provided evidence that both the forces in the bolt and the friction force stop increasing once the bolt has yielded.

Recent research conducted by Franceschetti and Denavit (2021) provides proposed formulas to evaluate tearout strength of bolted connections. The research summarized 471 specimens of single and multiple bolts in the database that failed in bearing and tearout. Among these specimens, only a few of them were fully pretensioned. This study also contains tension tests of 22 single-bolt butt splice connections with different hole types and edge distances. The test bolt was snug-tightened, and the plies were ensured to be in firm contact except for one specimen where grease was applied to the faying surfaces. The report observed that the greased specimen has a less stiff load-deformation curve compared to the snug-tightened specimen, and the strength of snug-tightened bolt at ¼ in. and ultimate deformation are 13% and 12% greater than the greased specimen.

To expand on this knowledge and better understand the behavior of bolted splices, research was conducted using finite element analysis to investigate the impact of bolt pretension on the bearing strength of bolted connections. The splice components considered as part of these analyses are steel bolted splice connections with single or double bolts, relying on the limit state of bolt bearing strength to resist the tension forces applied to the connected steel plates. The objective of these analyses was to capture the physical behavior of such connections under progressively increasing tension loading up to peak bearing strength, with a particular focus on understanding the evolution of the contribution of friction forces present between the splice plates due to bolt pretension. The subsequent discussion will highlight key factors that contribute to the reduction of clamping and friction forces in bolted splice connections as the applied loading is increased.

Additionally, the study explores the same behavior in bolted splices that would be used in composite plate shear wall/concrete filled (C-PSW/CF). This type of composite wall, which consists of two steel faceplates with a concrete core sandwiched between them, has been extensively investigated in past research (Agrawal, 2020; Alzeni, 2014; Alzeni and Bruneau, 2017; Kizilarslan, 2021; Kizilarslan and Bruneau, 2021, 2023; Sener and Varma, 2014; Shafaei et al., 2021; Varma et al., 2014), and is detailed in ASCE/SEI 7, *Minimum Design Loads and Associated Criteria for Buildings and Other Structures* (2022), the AISC *Specification* (2022b), and the AISC *Seismic Provisions for Structural Steel Buildings* (2022a). The national attention generated by implementations of C-PSW/CF in seismic regions has also led to interest for its use in nonseismic regions where bolted splices are preferred over welded splices. Consequently, numerical analyses have also been conducted to examine the effect of pretension on bearing strength in bolted composite splices.

FINITE ELEMENT MODELS

The section details the finite element models developed in LS-DYNA (Hallquist, 2006) to explore the relationship between friction and bearing in bolted connections for both all-steel and C-PSW/CF models.

All-Steel Bolted Connections

Analyses were first conducted on all-steel bolted connections. Figure 1 shows the geometries and finite element models of bolted splice connections relying on a single bolt or two bolts to transfer a tension loading applied to the steel plates, along with the reference coordinate system used for the analyses (X, Y, and Z directions). These models consist of faceplates, splice plates, and bolts (the term "faceplate" is used here by analogy with the splices in C-PSW/CF that will be addressed later). Table 1 outlines the geometries used in the finite element models considered. The table shows that the steel plate thickness, t (including faceplates and splice plates), and width, W, remain constant across all models. W_e is the net width of the connection, n denotes the number of bolts, d and d_h are the diameter of the bolt and the bolt hole, respectively, e is the edge distance from the bolt center to the plate edge, and S is the spacing between bolts. The term BR in the table refers to the bearing ratio, which can be expressed as shown in the following equation.

$$BR = \frac{A_e F_u}{ndtF_u} = \frac{W_e t F_u}{ndtF_u} = \frac{W_e}{nd} \tag{1}$$

Equivalently, BR can be defined as the net section area, A_e, divided by the total bearing area, ndt. Consequently, for a steel plate to have a net section rupture strength greater than a bearing strength of $3.0dtF_u$, the BR value must be larger than 3.0.

All steel (plates, bolts, etc.) was modeled using the plastic_kinematic (MAT_003) bilinear material model with kinematic hardening, as summarized in Table 2. In all the bolted connection models considered here, standard hole was used. The edge distance to bolt center, e, and center-to-center bolt spacing, S (as shown in Figure 1), have been chosen to prevent tearout being the controlling limit state.

Table 1. Geometries of Finite Element Models

Model	*t* (in.)	*W* (in.)	W_e (in.)	Rows	*n*	d_h (in.)	*d* (in.)	*E* (in.)	*S* (in.)	*BR*
1	0.375	6	4.875	1	1	1.125	1	4.00	—	4.875
2	0.375	6	4.875	2	2	1.125	1	4.00	4.00	2.438
3	0.375	6	5.188	2	2	0.8125	0.75	4.00	4.00	3.458
4	0.375	6	5.313	2	2	0.6875	0.625	4.00	4.00	4.250

Table 2. Material Properties for Steel Parts

Part	E_s (ksi)	Possion's Ratio	F_y (ksi)	F_u (ksi)	E_t (ksi)	β
Faceplates	29000	0.3	55	70	109	0.0
Splice plates	29000	0.3	55	70	109	0.0
Bolts/rods	29000	0.3	120	150	221	0.0

Using the AISC *Specification* (2022b), calculated strength for the limit states of bearing strength ($2.4dtF_u$ and $3.0dtF_u$), net section rupture strength (A_eF_u), gross section yielding strength (A_gF_y), and bolt shear strength are summarized in Table 3 for the finite element models considered. Single-bolt (Model 1) and double-bolt (Models 2–4) connections were considered. Three different bolt diameters were used in double-bolt connections (Models 2–4) to assess the influence of bending and shear deformation of bolts on the development of bearing strength. Except for Model 2 where net section failure occurs shortly after the onset of bearing deformations, all bolted connection models are governed by the bearing limit state.

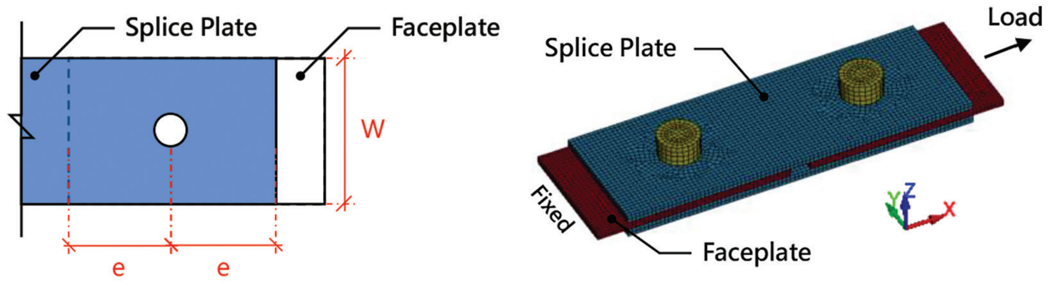

(a) Geometries and finite element model of single-bolt connection

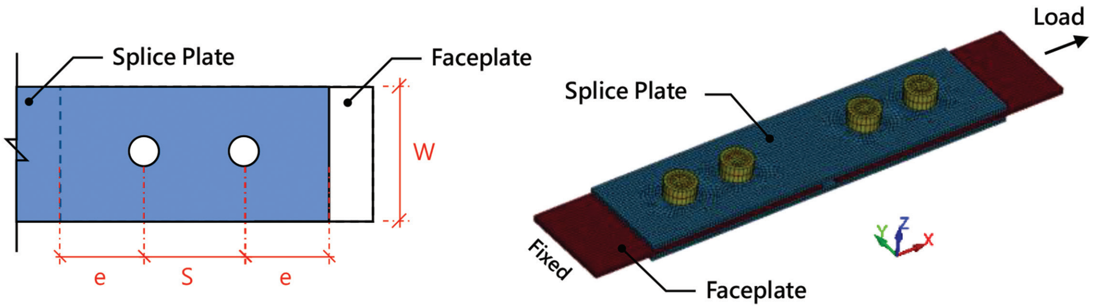

(b) Geometries and finite element model of double-bolt connection

Fig. 1. Finite element models.

Table 3. Design Limit States of Finite Element Models (Strength for Two Bolts in Cases 2, 3, and 4)

Model	A_eF_u (kips)	A_gF_y (kips)	$2.4dtF_u$ (kips)	$3.0dtF_u$ (kips)	Bolt Shear Strength (kips)	Governing Limit State
1	128	124	63.0	78.8	133	Bearing
2	128	124	126	158	265	Gross section yielding
3	136	124	94.5	118	149	Bearing
4	140	124	78.8	98.4	104	Bearing

For all finite element models analyzed, fixed boundary conditions were applied at one end, and a progressively increasing axial deformation was imposed at the other end to induce axial loading on the plates. Additionally, all bolts were preloaded to a stress equal to 105 ksi before any axial loading was applied to the plates. Figure 2 schematically shows the typical contact interfaces in the finite element models. These interfaces include the contact surfaces between steel plates, between bolts and steel plates, and between nuts and splice plates. All these contact interfaces in the analysis were specified using the automatic_surface_to_surface_mortar contact model with a static interface friction coefficient set to 0.3.

Bolted C-PSW/CF Connections

Three finite element models of bolted C-PSW/CF connections were built to study the clamping effect for bolted C-PSW/CF connections. Models T1 to T3, illustrated in Figures 3, 4, and 5, include the corresponding coordinate system (X, Y, and Z directions). These models consist of faceplates, splice plates, bolts or through rods with pipe-sleeves, tie bars, and infill concrete. The steel material model, contact model, and boundary constraints for these models were consistent with those used in the all-steel bolted connection models. The material properties for the steel elements in these bolted C-PSW/CF connection models are summarized in Table 4. The Winfrith concrete material model (MAT_085 in LS-DYNA) was used for concrete elements, as shown in Table 5.

The material model parameters include the elastic modulus, E_c, Poisson's ratio, the concrete compressive strength, f'_c, the concrete tensile strength, f_t, fracture energy, FE, and aggregate size, ASIZE. The same Poisson's ratio of 0.2 and aggregate size of 0.5 were used in all models. The material strengths of the steel plates and concrete were determined from 12 coupon tests and 15 concrete cylinder compressive tests, conducted during cyclic tension tests of the C-PSW/CF components with bolted splices (Liu and Bruneau, 2024). Table 6 provides information on the geometry of the bolted C-PSW/CF connections and includes details on the bearing ratio (BR), which ranges from 2.6 to 5.9 for the cases considered. The results from Models T1 and T2 are used to investigate friction development in scenarios where the connection is primarily governed by bearing strength. In contrast, Model T3 is utilized for comparison in situations where net section yielding occurs before the bearing strength of $2.4dtF_u$.

FRICTION FORCES IN STEEL BOLTED CONNECTIONS

Single-Bolt Connection (Model 1)

Figures 6(a) and 7(a) show the load-deformation curve obtained from the finite element analysis of Model 1 with and without applying bolt pretension. In these figures, deformation is measured from end-to-end of the model. The

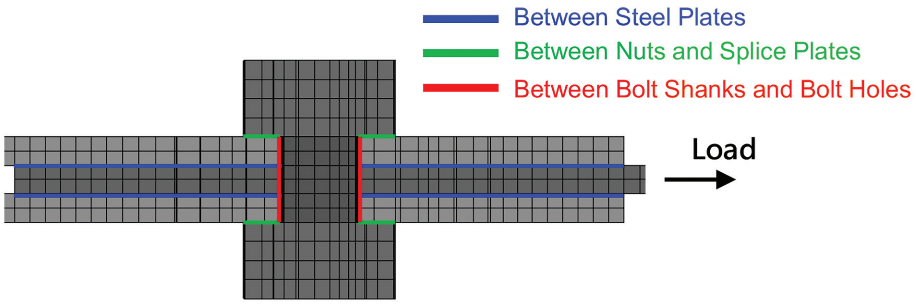

Fig. 2. Typical contact interfaces in the finite element model.

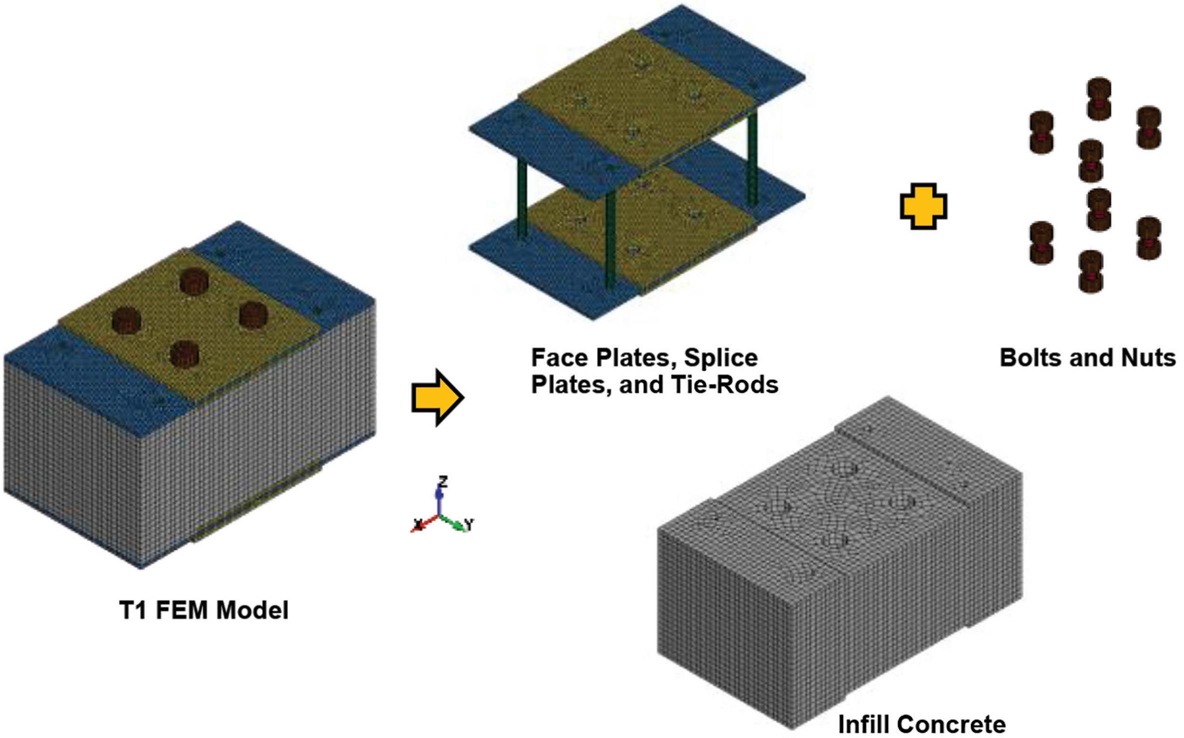

Fig. 3. Finite element model T1.

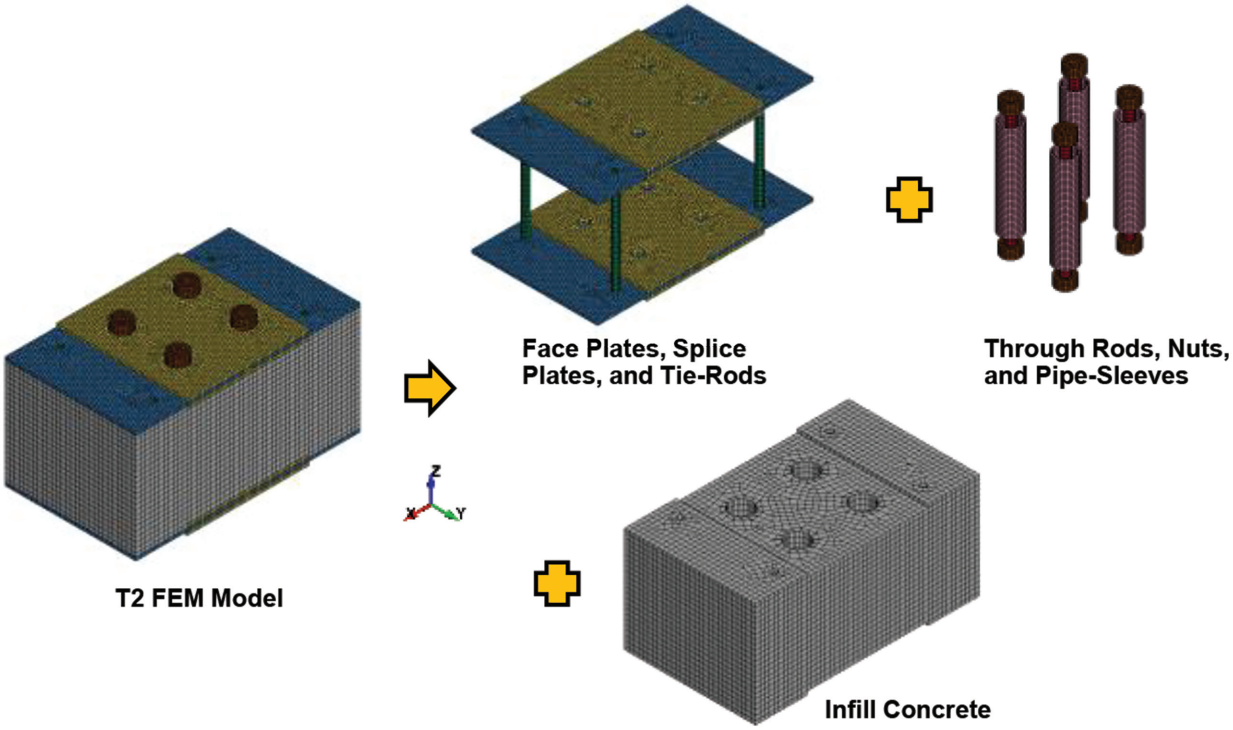

Fig. 4. Finite element model T2.

Table 4. Material Properties of Steel

Part	E_s (ksi)	Possion's Ratio	F_y (ksi)	F_u (ksi)	E_t (ksi)	β
Steel plates	29000	0.3	63.2	83.2	146	0.0
Bolts/rods	29000	0.3	120	150	221	0.0

Table 5. Material Properties of Concrete

Specimen	E_c (ksi)	Possion's Ratio	f_c' (psi)	f_t (psi)	FE	ASIZE
T1	4227	0.2	5500	550	0.00187	0.500
T2	4303	0.2	5700	570	0.00180	0.500
T3	4303	0.2	5700	570	0.00180	0.500

Table 6. Geometries of Models T1, T2, and T3

Specimen	t (in.)	W (in.)	W_e (in.)	Rows	n	d_h (in.)	d (in.)	e (in.)	S (in.)	BR
T1	0.375	14	11.750	1	2	1.125	1	4.00	—	5.875
T2	0.375	14	11.750	1	2	1.125	1	4.00	—	5.875
T3	0.375	14	9.875	1	3	1.375	1.25	4.00	—	2.633

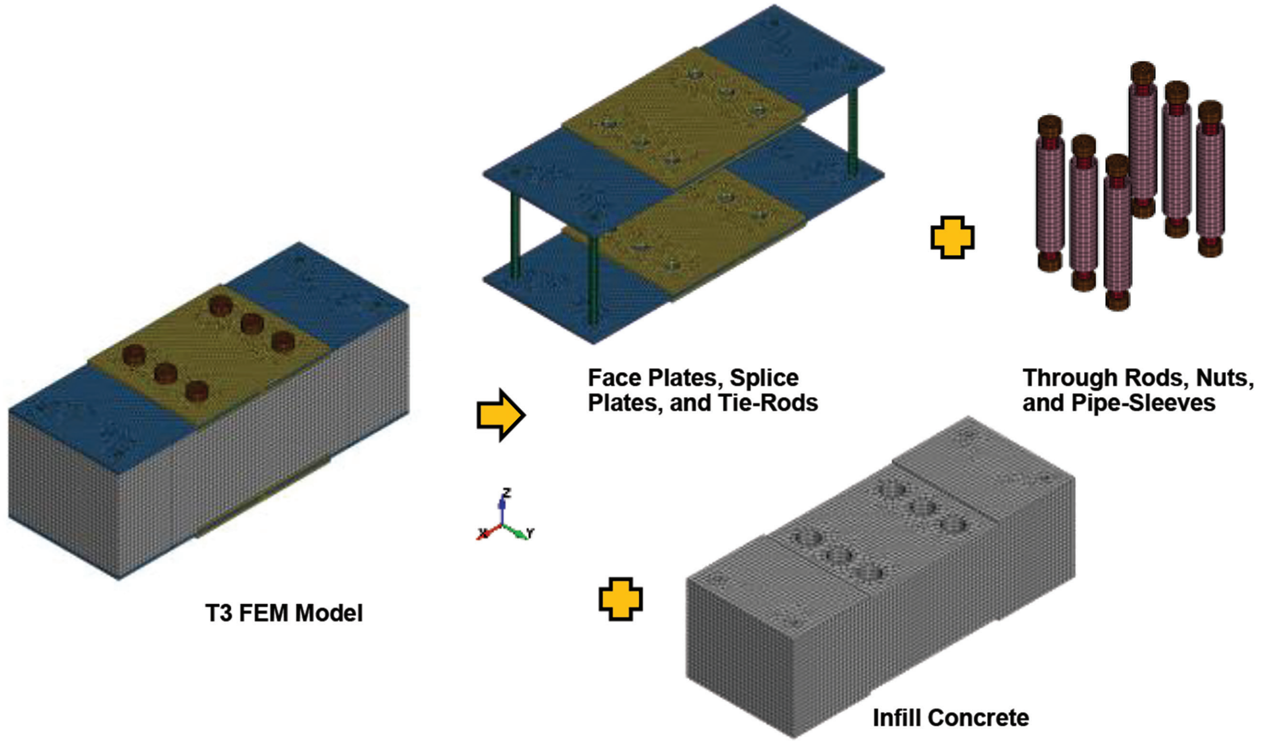

Fig. 5. Finite element model T3.

load-deformation curves compare the total axial force in the connection with the friction and bearing forces obtained from the contact interfaces. To evaluate the impact of the inelasticity of bolts on behavior, separate analyses were conducted, first with the material properties of the bolts modeled as elastic, and then using the inelastic bolt material properties listed in Table 2. Both results considering regular (i.e., inelastic) and elastic bolt material are shown in Figures 6(a) and 7(a).

For the bolted connection with bolt pretension (Figure 6), the preloaded stress is 105 ksi on 1-in.-diameter bolts, and the pretension force, T_b, is:

$$
\begin{aligned}
T_b &= \left(\frac{\pi}{4}\right)(1\text{ in.})^2(105\text{ ksi}) \\
&= 82.5\text{ kips}
\end{aligned}
$$

Therefore, the calculated slip resistance is:

$$
\begin{aligned}
2(\mu T_b) &= 2(0.3)(82.5) \\
&= 49.5\text{ kips}
\end{aligned}
$$

The value is close to the numerically obtained initial friction (51.6 kips) marked in Figure 6(a). The effective area of bolt shanks, accounting for threads, and the D_u factor were omitted for simplicity in calculating slip-critical resistance. This simplification results in an approximately 15% overestimation of the slip-critical resistance based on AISC *Specification* Equation J3-4.

After the connection slid, the bearing force started to develop. It can be observed that as the bearing force and deformations increased, the friction force decreased simultaneously. At a deformation of 2.0 in., the maximum axial forces for regular and elastic bolt models reached 104 kips and 109 kips, while the maximum bearing forces reached 88.7 kips and 80.5 kips, respectively. The residual friction forces for regular and elastic bolt models were 17.5 kips and 30.4 kips at 2.0 in. deformation, representing 34% and 59% of the initial friction force, respectively. By comparing the regular and elastic bolt material, there is an approximate 25% loss (59% − 34%) of friction force due to the partial yielding of bolts.

For the bolted connection without bolt pretension, as shown in Figure 7(a), sliding occurred immediately after applying the axial load. After sliding, the bearing and friction forces developed simultaneously, with friction induced as a consequence of bearing. Similarly, the load-deformation curve shows the analysis results from both regular and elastic bolt models. The maximum axial forces in the regular and elastic bolt models reached 104 kips and 112 kips at 2.0 in. deformation, while the corresponding maximum bearing forces were 81.4 kips and 89.2 kips, respectively. The maximum friction forces reached 28.0 kips at 0.73 in. deformation and 37.6 kips at 1.03 in. deformation in the regular and elastic bolt models. The residual friction forces at 2.0 in. deformation were 16.2 kips and 32.2 kips in the regular and elastic bolt models, respectively, which are values nearly identical to the case with pretension.

Figures 6(b) and 7(b) show the relationship between total deformation (labeled “deformation”) and hole elongation for Model 1 for the case of regular bolt material. Note that the vertical axis in these figures represents the sum of hole elongation from both sides of the splice. Both figures show

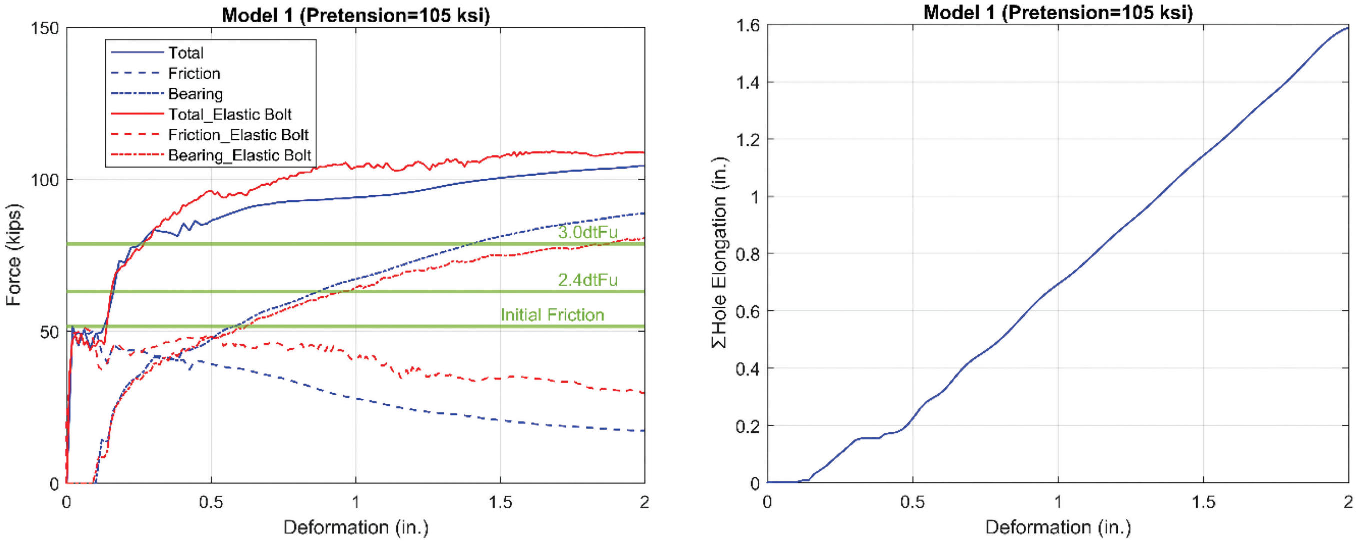

(a) Load-deformation curve *(b) Deformation vs. hole elongation*

Fig. 6. Analysis result of Model 1 (with pretension).

that hole elongation contributed to approximately 80% of the total deformation (measured between the two ends of the model). With pretension (Figure 6), when the axial load reached the bearing strength of 2.4dtF_u, the total deformation was 0.16 in, corresponding to sum of hole elongation of 0.03 in. When the bearing force alone reached 2.4dtF_u, the total deformation was 0.87 in., corresponding to a sum of hole elongation of 0.6 in. For comparison, without pretension (Figure 7), at the same bearing strength of 2.4dtF_u, the total deformation was 0.43 in, corresponding to a sum of hole elongation of 0.17 in. When the bearing force alone reached 2.4dtF_u, the total deformation was 0.85 in., corresponding to a sum of hole elongation of 0.55 in. Sum of hole elongation of 0.55 to 0.6 in. corresponds to individual hole elongation of half those values. This suggests that without friction, the bolt hole elongation at the bearing strength of 2.4dtF_u in Model 1 is close to the 0.25 in. elongation observed in the tests by Frank and Yura (1981).

Further analysis of the results was performed to identify the causes for this progressive reduction in friction forces. Figure 8 shows the von Mises stress distribution in the connection at different deformation stages, illustrating the growth of the yielding "field" in the faceplate as hole elongation increases. Figure 9 shows typical deformations of this single-bolt connection at 2.0 in. deformation. The observed deformations in both figures around the bolt include hole elongation, thickness changes in the plates, and bending of plates and bolts.

A free-body diagram of the connection system showing contact springs is presented in Figure 10. In this diagram, nuts, splice plates, and faceplates are interconnected by contact springs, forming a system of springs in series. The spring constant is determined based on the stiffness factor, k_i, defined in the LS-DYNA theory manual (Hallquist, 2006). The stiffness factor, k_i, is given in terms of the bulk modulus, K_i, the volume, V_i, and the face area, A_i, in the contact interface. Based on the findings from Kizilarslan and Bruneau (2023) and Polat and Bruneau (2018), it was recommended that the contact stiffness in the model be set to 10 ($f_{si} = 10$) to prevent slippage of the concrete core under large deformations. Note there is no gap for the contact spring in the bolted connection studied here. Upon applying axial deformations to the connection, relative movements develop between the plates, and the faceplate undergoes substantial hole elongation, as illustrated in Figure 11. As this occurs, the initial contact spring loses contact area and contact stiffness due to hole elongation and thinning of the faceplate in tension due to Poisson's effect (Figure 12). Figure 13 highlights the thickness change around bolt holes in the spliced plate at three different positions (P1, P2, and P3, respectively located at the left, middle, and right end of the bolt hole), and Figure 14 shows the thickness change along with the axial deformation of the connection. These show an increase in the spliced plate thickness as it is compressed by the bolts in bearing. This increase in the thickness of the faceplate at the bolt bearing point increases the distance between the bolt head and the nut on that one side of each bolt, resulting in bolt bending and yielding (Figure 15). These factors collectively influence the behavior of the contact springs on both sides of the bolt. A net reduction in contact forces results in decreased clamping and friction forces. These behaviors contribute significantly to the reduction in friction observed across all finite element models.

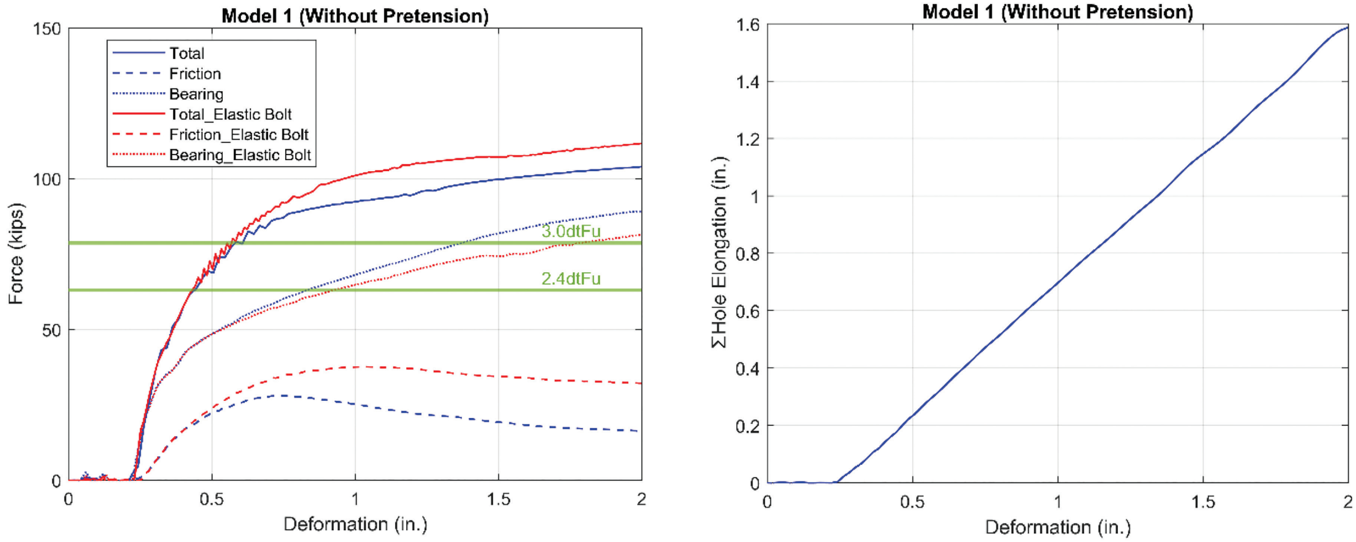

(a) Load-deformation curve *(b) Deformation vs. hole elongation*

Fig. 7. Analysis result of Model 1 (without pretension).

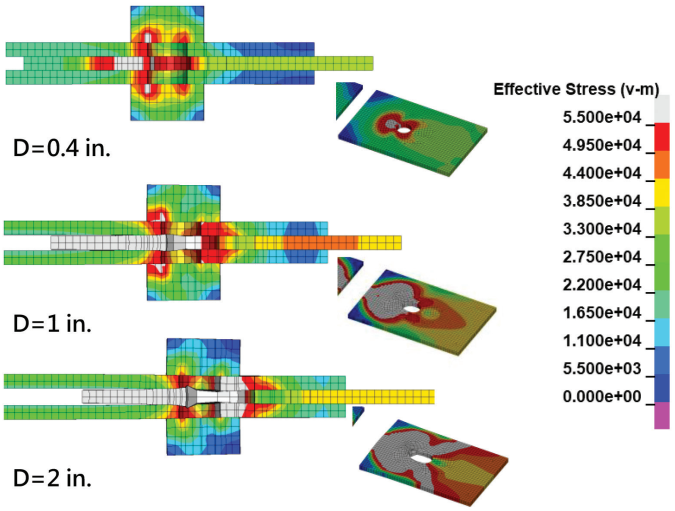

Fig. 8. Von Mises stresses of Model 1 at different deformations (bolt shank not shown).

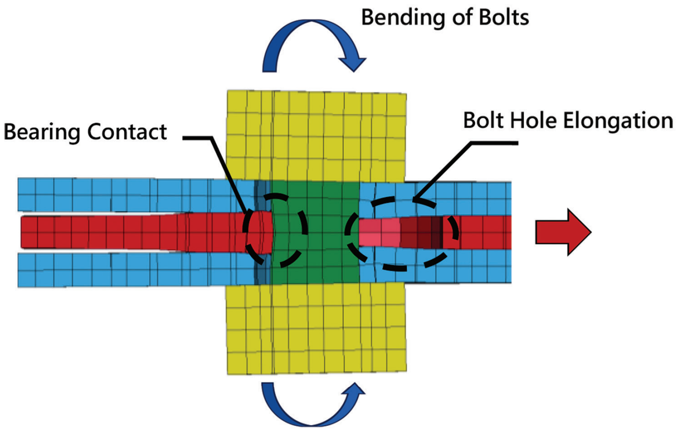

Fig. 9. Deformation around bolts of Model 1 (deformation = 2 in.).

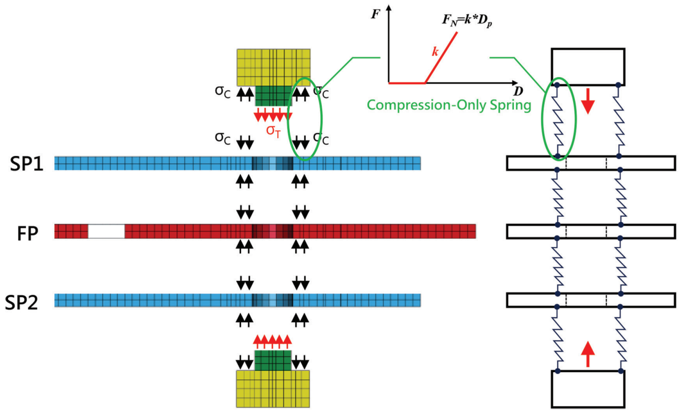

Fig. 10. Free-body diagram of spring system of bolted connections (preload stage).

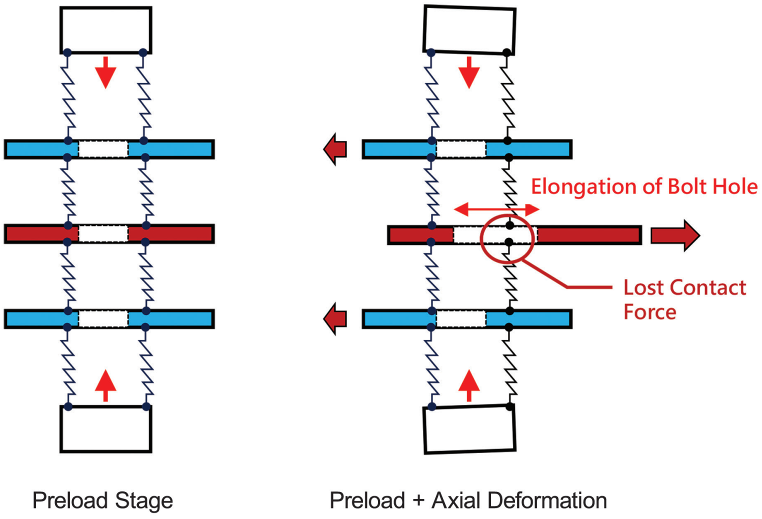

Fig. 11. Free-body diagram of spring system of bolted connections (preload and deformed stages).

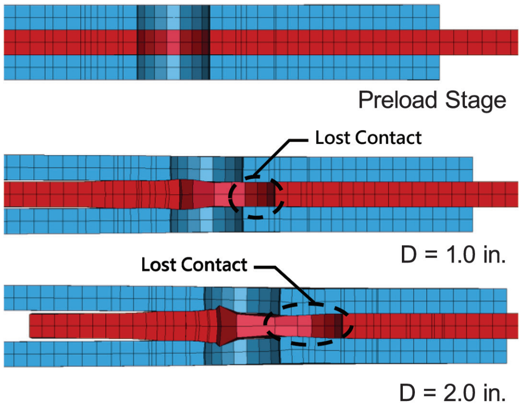

Fig. 12. Deformation of connection Model 1 (bolts not shown).

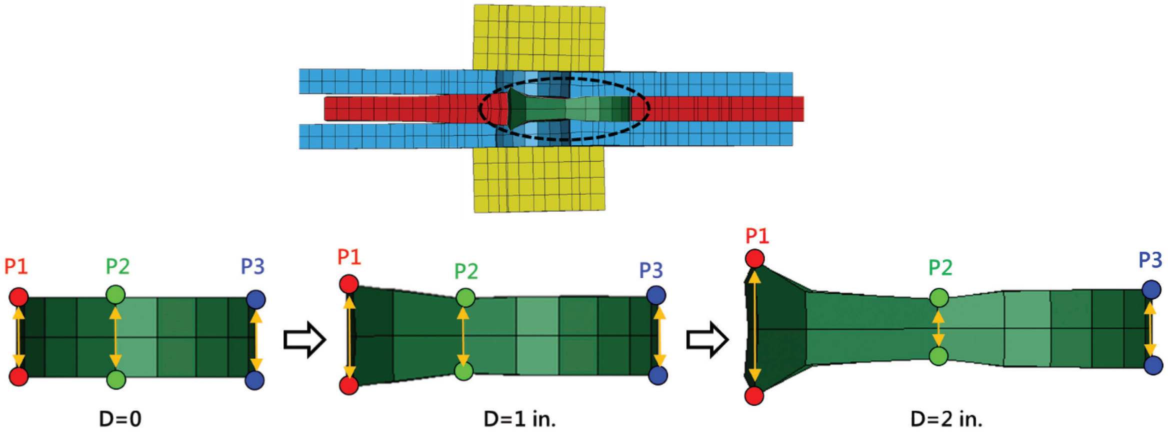

Fig. 13. Thickness change around bolt holes (Model 1).

Figure 16 shows the history of clamping stress vectors at different values of connection axial deformation. For the reasons mentioned earlier, the clamping stress vectors on the right (the side where the hole elongates in that figure) lost contact area and stiffness, resulting in a significant reduction in magnitude of the stress vectors with the application of axial deformation. Simultaneously, the thickness of the faceplate around the bolt hole became thinner there, leading to reduced clamping stresses around the bolt hole. Figures 17 and 18 show the 2D distribution of these clamping and friction stress vectors on a splice plate and the faceplate, respectively. Similarly, the clamping stress vectors are shown to significantly reduce as hole elongation increase. Figure 19 shows the variation in the clamping force and bolt tensile force as a function of bolt hole elongation. The clamping force decreased from initial value of 85 kips to 31 kips as the hole elongated to 0.8 in. deformation, and the axial force in the bolt correspondingly reduced by the same amount.

Double-Bolt Connection (Model 2 to Model 4)

As mentioned earlier, Models 2, 3, and 4 were used for investigating the clamping effect considering various bolt diameters (1 in., ¾ in, and ⅝ in. in Models 2, 3, and 4, respectively), with a *BR* ranging from 2.44 to 4.25. As previously noted in Figure 9, Model 1 exhibited some bolt bending behaviors. Consequently, there was interest in exploring

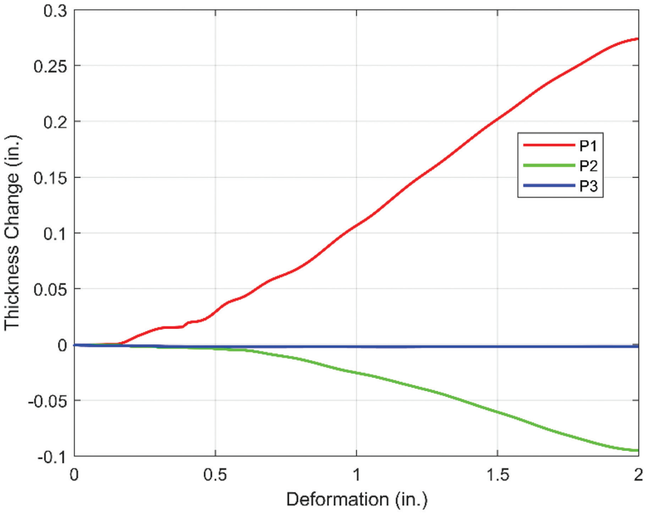

Fig. 14. Thickness change around bolt holes (Model 1).

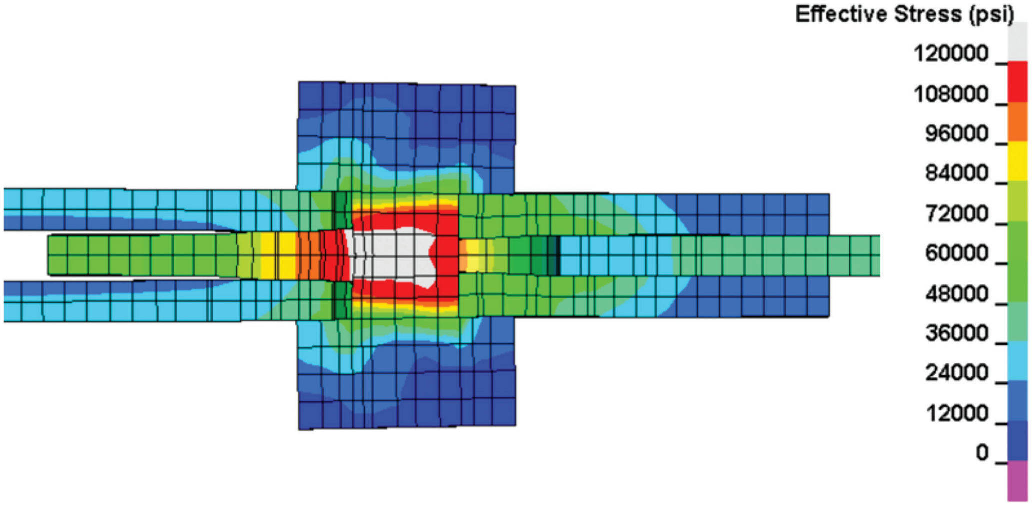

Fig. 15. Bending and yielding of bolts (Model 1).

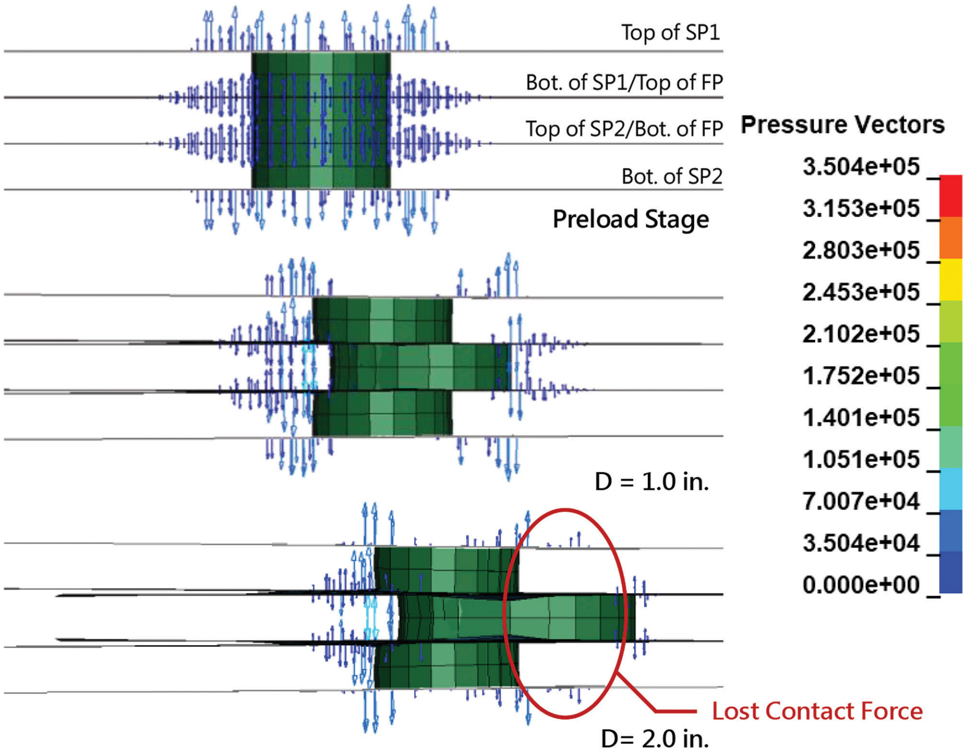

Fig. 16. Elevation views of contact interfaces showing clamping stress vectors (Model 1).

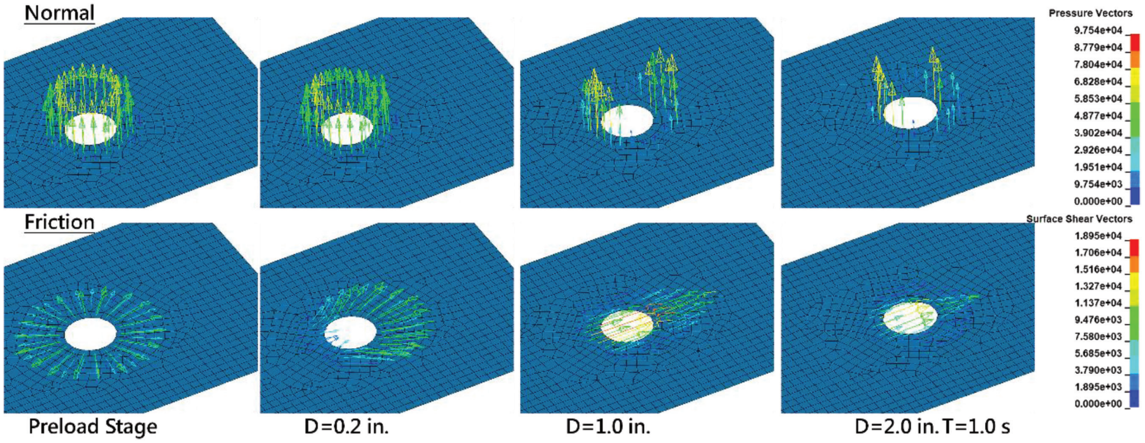

Fig. 17. Normal and friction stresses on the surface of the splice plate (Model 1).

this behavior under double-bolt connections in Models 2–4. The aim was to assess whether the bending of bolts will be mitigated in these configurations and to understand the influence on the development of friction. Figures 20–22 show the load-deformation curves of the finite element analysis for Models 2–4. Table 7 provides the calculated slip resistance for the models.

In Model 2 (Figure 20), the calculated slip resistance and numerically obtained initial friction force are 99.0 and 97.7 kips, respectively. After the connection slip, the bearing force started to develop, reaching its maximum value at the end of the analysis (arbitrarily stopped at 2.0 in. deformation). As mentioned in Table 3, the governing limit state in Model 2 is gross section yielding. Accordingly, the total axial force reached a plateau near 120 kips after 0.4 in. deformation, closely approaching the gross section yielding strength. The peak total axial force reached 125 kips at a deformation of 2.0 in., exceeding the gross section yielding strength of 124 kips and approaching the bearing strength of $2.4dtF_u$, set at 126 kips. At 2.0 in. deformation, the residual friction force is 40 kips, representing a 59% reduction compared to the initial friction force. When comparing Models 1 and 2, both featuring 1 in. bolt diameters and including single-bolt and double-bolt connections, it is observed that the residual friction in Models 1 and 2 is 34% and 41% of their initial friction force, respectively. This suggests that there is a greater reduction in friction in single-bolt connections compared to double-bolt connections under large bolt hole deformation due to bearing.

In Model 3 (Figure 21), the calculated slip resistance and numerically obtained initial friction force are 55.7 and 52.7 kips, respectively. The bearing force developed after connection slip, and it reached $2.4dtF_u$ at 0.8 in. deformation. Concurrently, the total axial force reached the bearing strength of $2.4dtF_u$ at a deformation of 0.23 in., and it achieved the bearing strength of $3.0dtF_u$ at a deformation of 0.89 in. The peak total axial force reached 127 kips at 2.0 in. deformation, which is larger than the gross section yielding strength of 124 kips. Meanwhile, the residual friction force was 18 kips, representing a 66% reduction compared to the initial friction force.

Finally, for Model 4 (Figure 22), the calculated slip resistance and initial friction force are 38.7 and 37.0 kips, respectively. The bearing force developed after connection slip, and it reached $2.4dtF_u$ and $3.0dtF_u$ at 0.51 and 0.81 in. deformations. Meanwhile, the total axial force attained the bearing strength of $2.4dtF_u$ at a deformation of 0.29 in., and it achieved the bearing strength of $3.0dtF_u$ at a deformation of 0.61 in. The peak total axial force attained 126 kips at 2.0 in. deformation, surpassing the gross section yielding strength of 124 kips. At that point, the residual friction force was 8 kips, representing a 78% reduction compared to the initial friction force. Table 8 compares Models 2–4, which have bolt diameters of 1.0, ¾, and ⅝ in., respectively. It lists the maximum axial forces at a 2.0 in. deformation as well as the initial and residual friction forces. Notably, the residual friction forces in Models 2–4 are 40, 18, and 8 kips, respectively, representing 41%, 34%, and 22% of their respective initial friction forces. The data show that smaller bolt diameters lead to greater reductions in friction due to their increased bending and shear deformations in bolted connections.

Figures 23–25 show the von Mises stresses distribution of these models at different deformation stages, highlighting the progressive yielding on the plates. As previously noted, the peak axial forces in Models 2–4 reached the

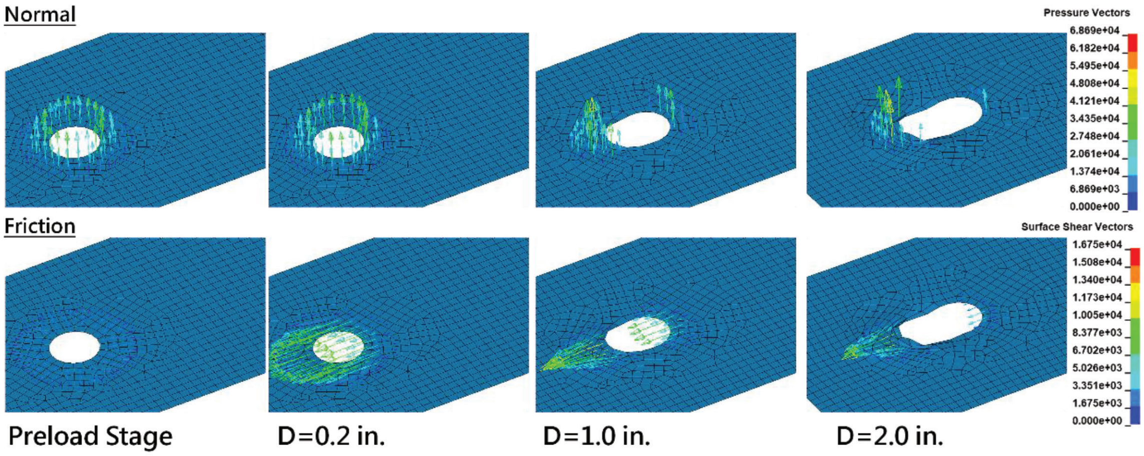

Fig. 18. Normal and friction stresses on the surface of the faceplate (Model 1).

gross section yielding strength, leading to observable whole section yielding around the inner bolts. In contrast, Model 1, which features a single-bolt connection and is shown in Figure 8, did not achieve its gross section yielding strength. In this model, yielding initiated around the bolt and extended toward the free edge, illustrating a different pattern of bearing stress distribution compared to the double-bolt connections.

Figure 26 shows the deformation of double-bolt connections (Models 2–4) at 2.0 in. deformation. Recall that these models have various bolt diameters, equal to 1, ¾, and ⅝ in. in Models 2, 3, and 4, respectively. It is noticeable that as the bolt diameter decreases, the bolt shanks exhibit more pronounced bending behavior (although, in Model 2, behavior was more dominantly governed by plate yielding rather than bolt bearing). Figure 27 shows the deformation of Model 3 (design governed by bearing) without showing the bolt shanks, providing a clearer view to observe the thickness change around bolt holes at locations identified as Bolt 1 and Bolt 2 in the figure. It can be observed that the bolt hole elongation is larger at location Bolt 1 (closer to the edge of splice plates), while the elongation is smaller at location Bolt 2 (closer to the center of the splice plates).

Recall from Figure 11, that as axial deformations are applied to the connection, relative movements occur between the plates, resulting in significant hole elongation in the faceplate. Figures 28–30 show the history of clamping stress vectors over axial deformation in Models 2–4. In the case of Model 2, where the design is governed by gross section yielding, the hole elongation of Bolt 2 is significantly less than that of Bolt 1. Therefore, the reduction of clamping stress vectors at Bolt 2 is less significant than at Bolt 1. Conversely, in Models 3 and 4, where the design is governed by bearing with smaller diameters of bolts, the bolts experience more bending, and the bolt holes have larger elongations, resulting in a more significant loss of clamping stress vectors. This phenomenon can also be observed by plotting the clamping force to hole elongation curves as shown in Figures 31–33. Also, the same conclusions were found by observing the clamping and friction stress vectors on the splice plate and faceplate as shown from Figures 34–39.

FRICTION FORCES IN BOLTED C-PSW/CF CONNECTIONS

Bolted C-PSW/CF Connections in Tension

Six cyclic C-PSW/CF components with bolted splices were tested by Liu and Bruneau (2024) to investigate the cyclic axial behavior of such splices in composite members. Results from the three specimens (T1–T3), for which bearing strength was the governing limit state, have been used here for comparison with the finite element analyses to investigate the impact of bolt pretension in this application.

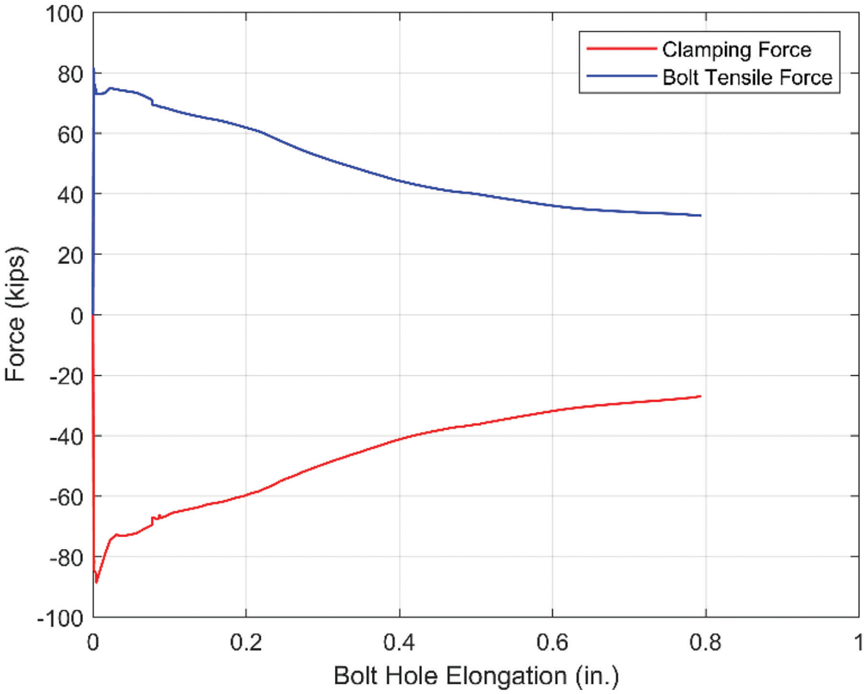

Fig. 19. Clamping force and bolt hole elongation curve (Model 1).

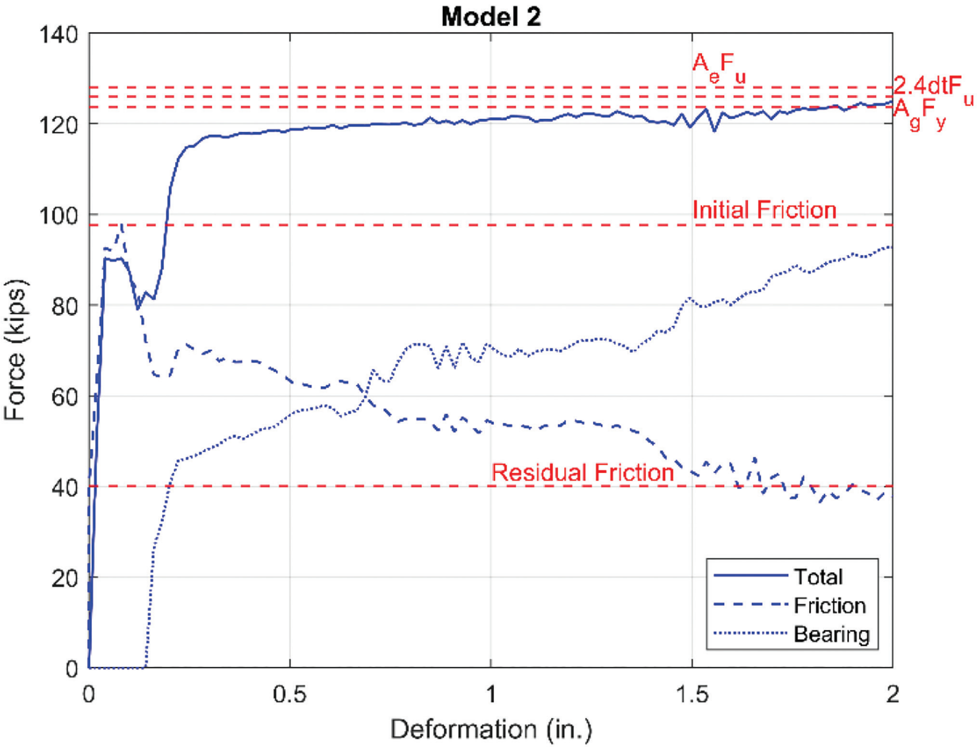

Fig. 20. Total axial force and friction force of Model 2.

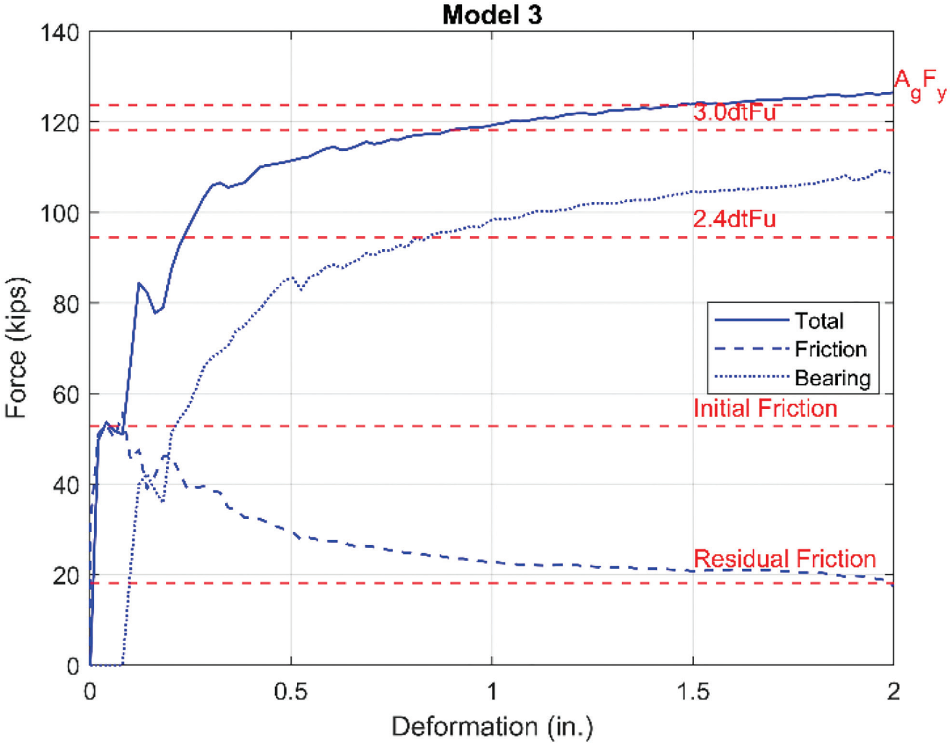

Fig. 21. Total axial force and friction force of Model 3.

Table 7. Calculated Slip Resistance for Models 2, 3, and 4

Model	Pretension T_b (kips)	Slip Resistance (kips)
2	82.5	99.0
3	46.4	55.7
4	32.2	38.7

Table 8. Initial and Residual Friction Forces in Models 2, 3, and 4

Model	Maximum Axial Force (kips)	Initial Friction Force (kips)	Residual Friction Force (kips)
2	125	97.7	40.0
3	126	52.7	18.0
4	125	37.0	8.0

Figures 40–42 present analysis results for Models T1–T3 (defined previously), showing the total axial forces and friction forces as a function of axial deformation. In these figures, the blue lines represent the results obtained from cyclic tension tests of the CPSW/CF components with bolted splices (Liu and Bruneau, 2024). The FEM analysis considers different pretension values in the bolts or through rods of the C-PSW/CF connections, with corresponding test results included in the figures. More specifically, the analyses of Models T1–T3 consider three pretension stress values—namely, 0 ksi (no pretension), 52.5 ksi (50% pretension), and 105 ksi (full pretension). These values correspond to axial forces of 0, 41.23 kips, and 82.5 kips for the 1-in.-diameter bolts/rods used in Models T1 and T2, and 0, 64.4 kips, and 129 kips for the 1¼-in.-diameter rods used in Model T3.

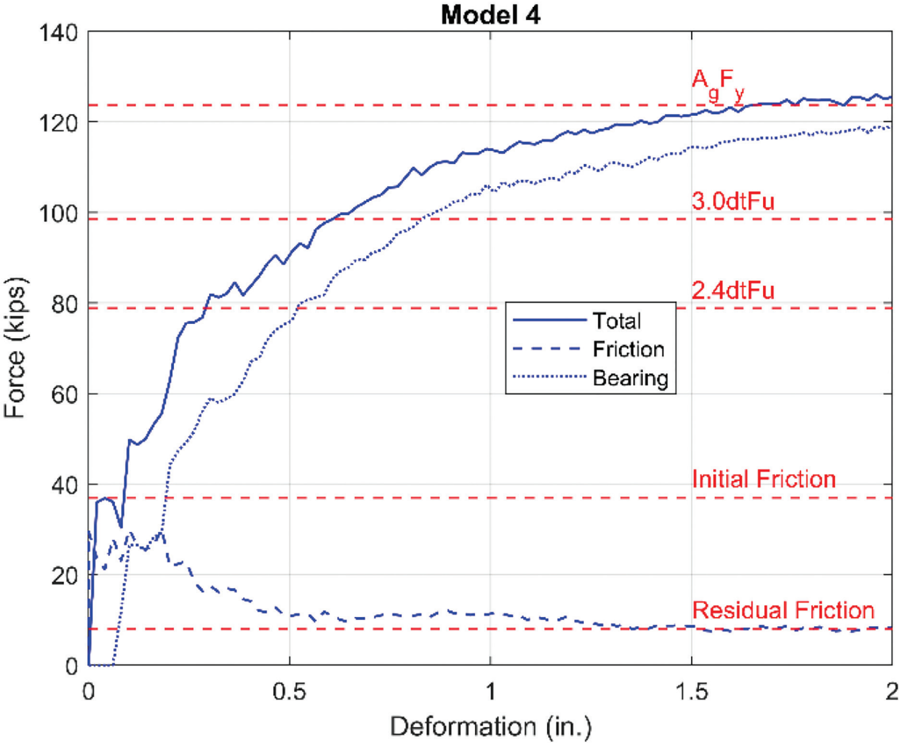

Fig. 22. Total axial force and friction force of Model 4.

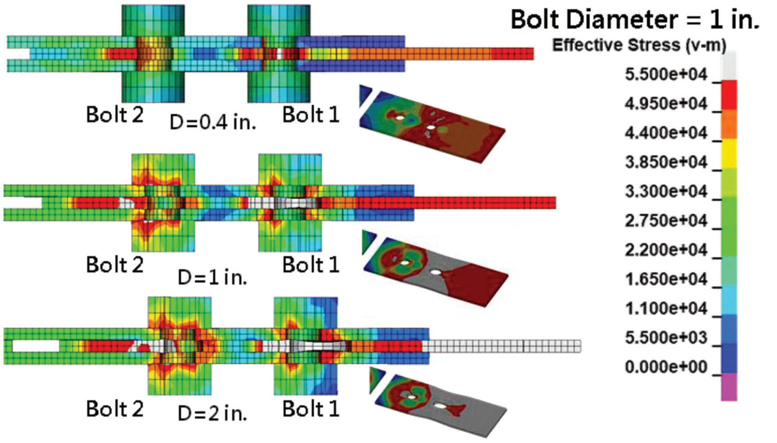

Fig. 23. *Von Mises stresses of Model 2 at different deformations (bolt shank not shown).*

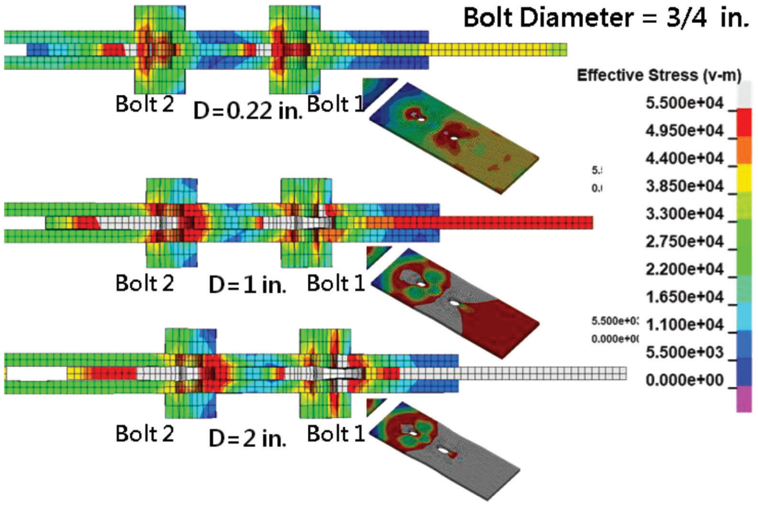

Fig. 24. *Von Mises stresses of Model 3 at different deformations (bolt shank not shown).*

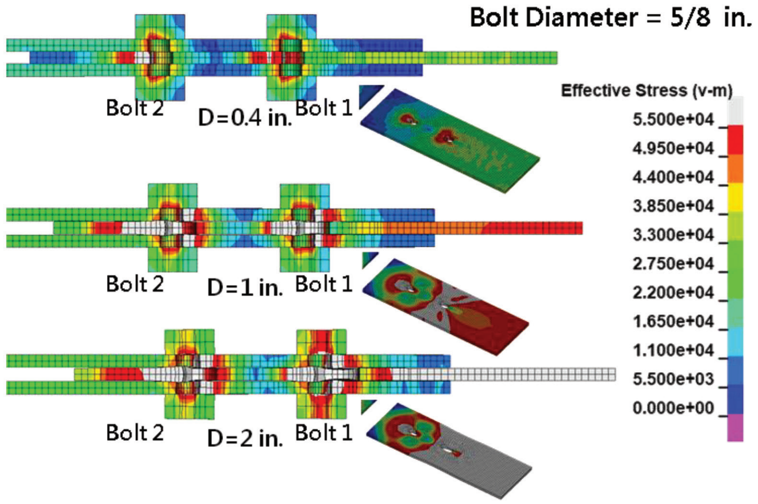

Fig. 25. *Von Mises stresses of Model 4 at different deformations (bolt shank not shown).*

The behaviors of steel bolted connections and C-PSW/CF bolted connections in tension show similarities. In both types, the bearing force begins to develop after connection slip, and the friction force starts decreasing following the development of the bearing force. In Models T1 and T2 (bearing-controlled case), the total axial forces reached $2.4dtF_u$ and $3.0dtF_u$ at axial deformations of approximately 1.3 and 1.2 in., regardless of the applied pretension values. For Model T3 (net section yielding-controlled case), the peak axial load reached net section yielding strength A_eF_y at deformations of 0.2, 0.55, and 0.82 in., for the cases of bolts pretensioned to values of 105, 52.5, and 0 ksi, respectively. The axial loads in the models plateaued after reaching net section yielding. Subsequently, regardless of pretension values, the axial load reached the bearing strength of $2.4dtF_u$ at deformation of 1.5 in.

While the curves indicate a significant drop in friction forces as axial deformation increases, regardless of the initially assigned pretension value, it can be observed there is no significant difference in the residual friction forces among each model under large axial deformation of connections—that is, when the connections reach their maximum bearing strength. Figure 43 shows the development of clamping stress vectors in Model T2, exhibiting a reduction behavior similar to the one described in the case of pure steel bolted connections. Figure 44 shows the clamping force versus bolt hole deformation curve for Models T1–T3, each under a pretension value of 52.5 ksi. The initial clamping forces for Models T1–T3 are 38, 38, and 55 kips,

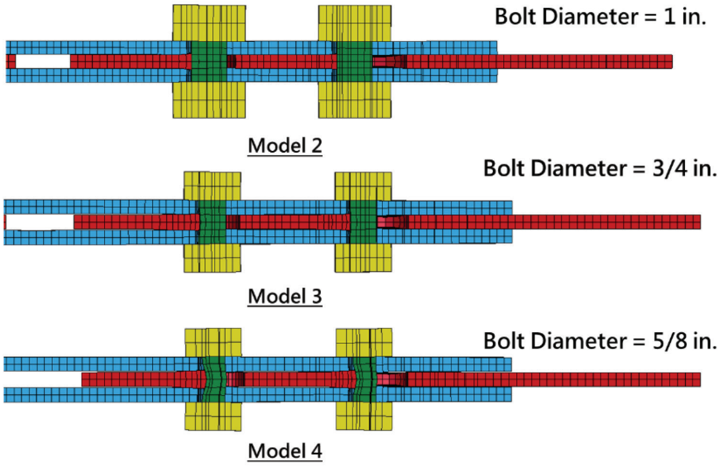

Fig. 26. Deformation of double-bolts connections (deformation = 2.0 in.).

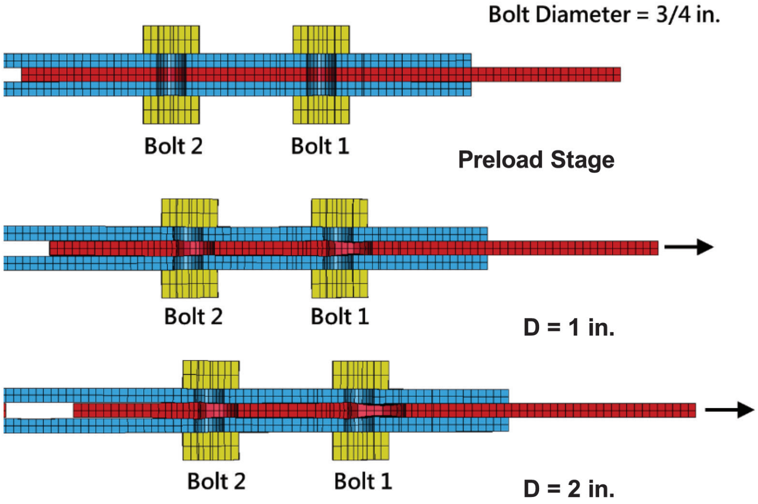

Fig. 27. Deformation of connection Model 3 (bolts shank not shown).

while the residual clamping forces are 16, 18, and 30 kips, respectively, representing 42%, 47%, and 55% of the initial clamping force. Models T1 and T2 show similar reductions in clamping force, likely due to having identical bolt numbers and diameters. Model T3 exhibits a smaller reduction in clamping force, likely due to its lower *BR*.

Bolted C-PSW/CF Connections in Compression

When a C-PSW/CF bolted connection is in compression, the high strength and stiffness of concrete contribute significantly to the axial load capacity. Model T1 was chosen to numerically explore the friction force that develops in the bolted splice region between the steel components as well as between the steel and concrete when the C-PSW/CF connection is in compression. The pretension value of this model was set at 55 ksi for 1-in.-diameter bolts. To simulate the lateral confinement in real wall scenarios, an additional side restraint was applied to the models.

Figure 45 shows the load-deformation curves obtained from the finite element analysis of Model T1 in compression in terms of the total axial force, the axial force in steel, and the axial force in concrete. The steel plates started sliding at a deformation of −0.01 in, corresponding to an axial load in the steel equal to 100 kips (labeled as P_1 in the figure), and the concrete resisted 261 kips (70% of the total axial load). At this point, the total axial load, P_{T1}, reached −372 kips. For comparison, the theoretical axial load in steel and concrete, P_{S1} and P_{C1}, predicted using relative elastic stiffness are:

$$\mathrm{PT1} = -372 \text{ kips} \tag{2}$$

$$P_{S1} = P_{T1}\frac{E_s A_s}{E_s A_s + E_c A_c} \tag{3}$$
$$= -85.6 \text{ kips}$$

$$P_{C1} = P_{T1}\frac{E_c A_c}{E_s A_s + E_c A_c} \tag{4}$$
$$= -286 \text{ kips}$$

where the Young's modulus of steel and concrete, E_s and E_c, are equal to 29,000 ksi and 4,227 ksi, respectively, and the area of steel and concrete, A_s and A_c, are 7 in.^{2} and 161 in.^{2}, respectively.

The member axial stiffness did not change significantly after sliding of steel plates started, and the concrete alone resisted the additional axial load. At a deformation of −0.04 in, when the total axial load reached −993 kips (labeled as P_2 in Figure 45), some concrete cracks were observed at this point as the infill concrete elements reached its compressive strength (5,500 psi), as shown in Figure 46, leading to a significant change in axial stiffness. At that point, the concrete resisted −871 kips, which is 88% of the total applied axial load. Peak strength for the connection

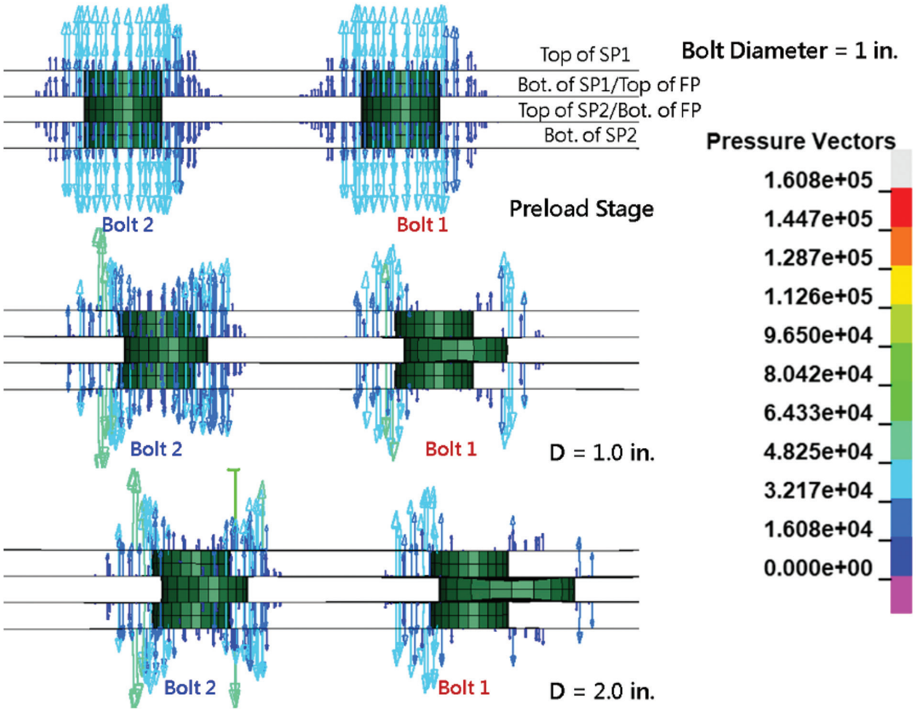

Fig. 28. Elevation views of contact interfaces with clamping stress vectors (Model 2).

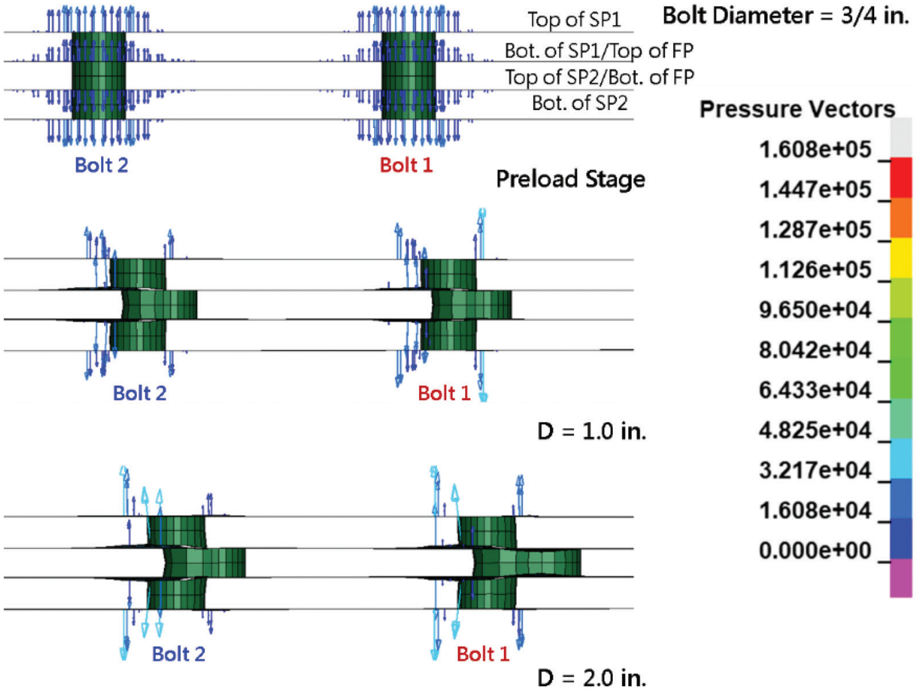

Fig. 29. Elevation views of contact interfaces with clamping stress vectors (Model 3).

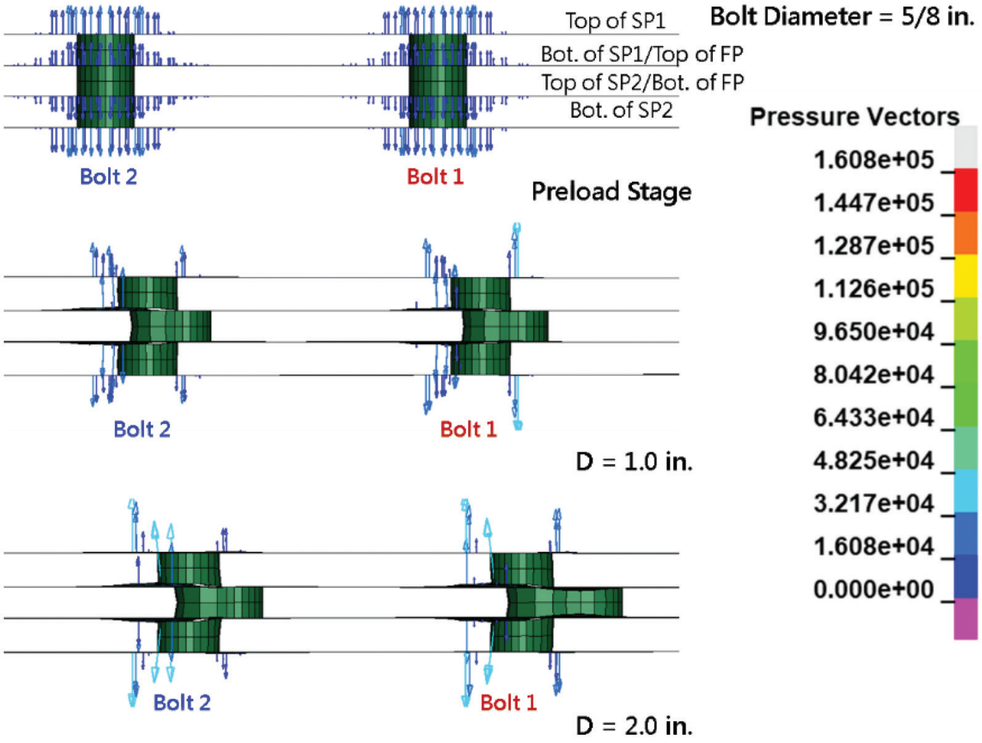

Fig. 30. Elevation views of contact interfaces with clamping stress vectors (Model 4).

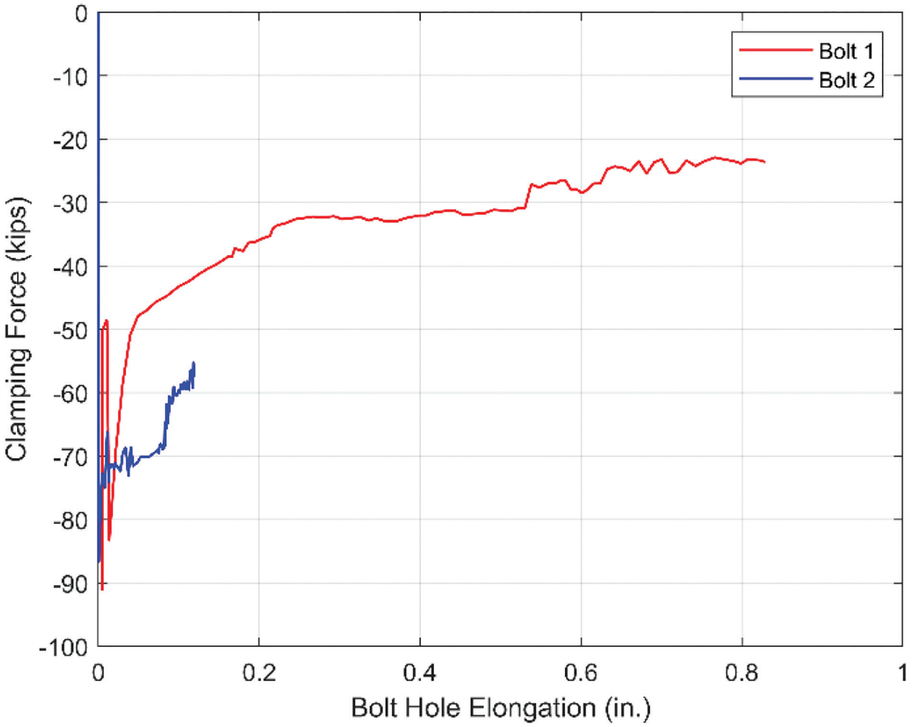

Fig. 31. Clamping force and bolt hole elongation curve (Model 2).

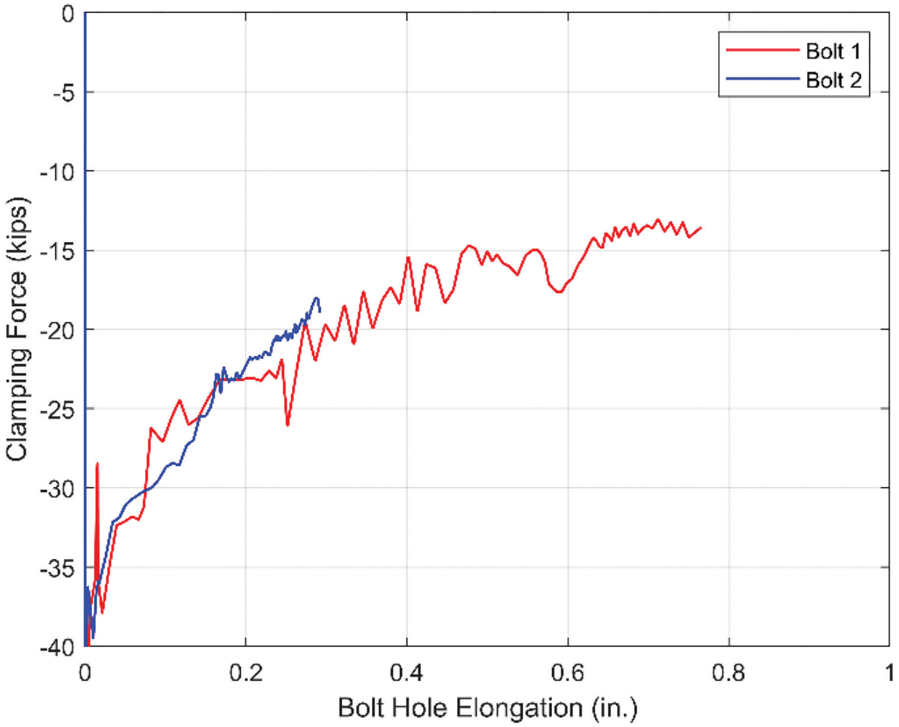

Fig. 32. Clamping force and bolt hole elongation curve (Model 3).

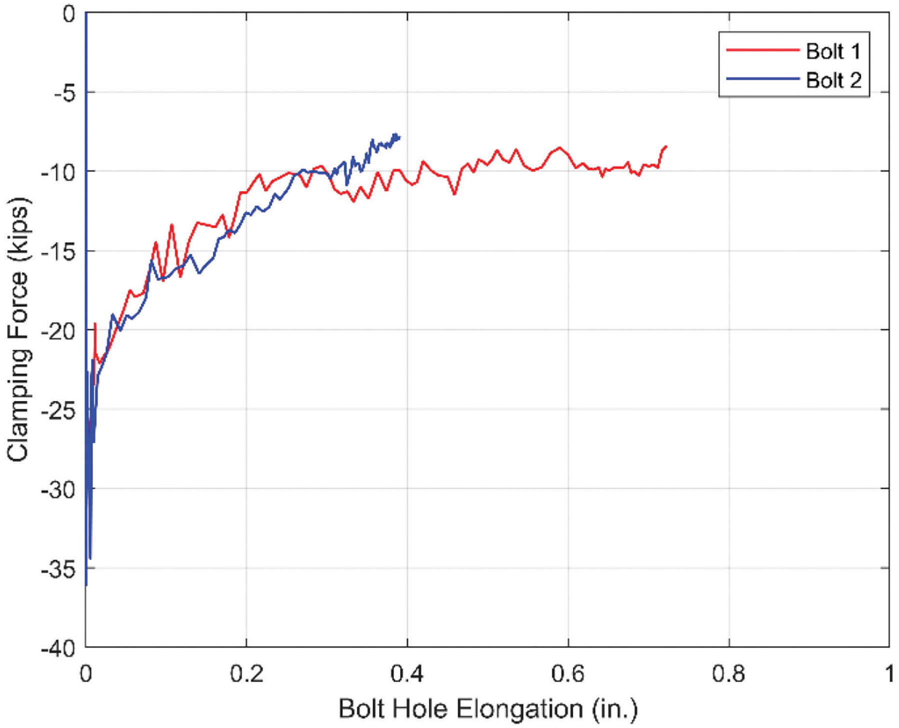

Fig. 33. Clamping force and bolt hole elongation curve (Model 4).

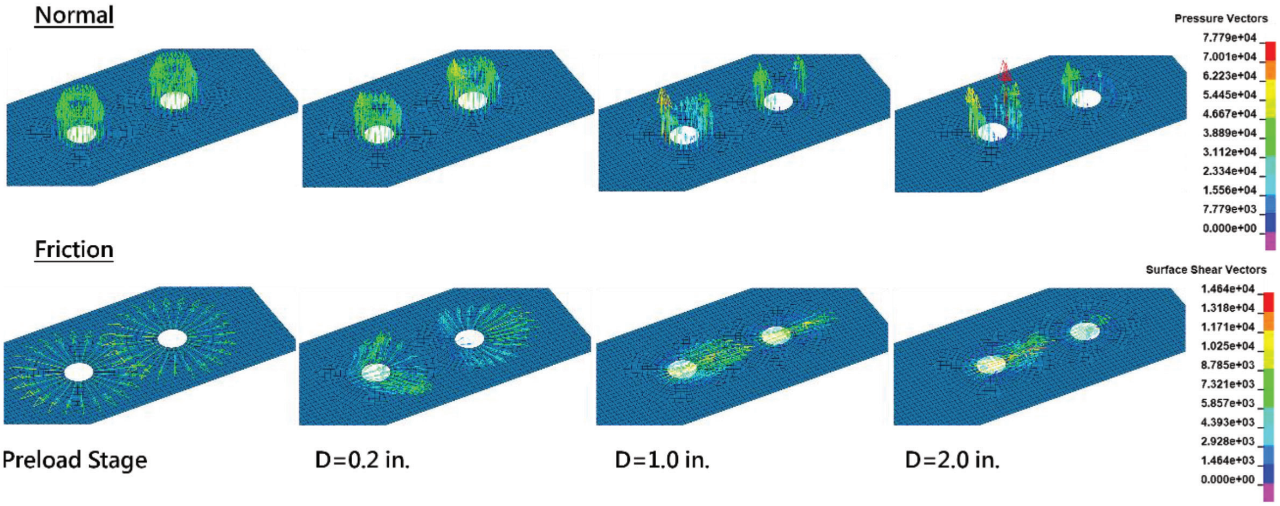

Fig. 34. Normal and friction stresses on the surface of the splice plate (Model 2).

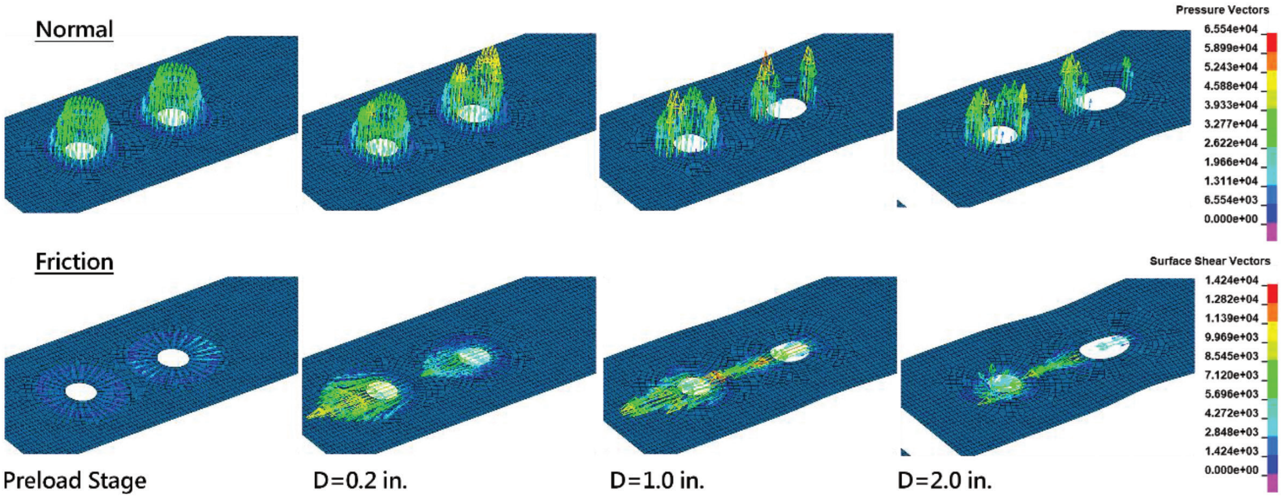

Fig. 35. Normal and friction stresses on the surface of the faceplate (Model 2).

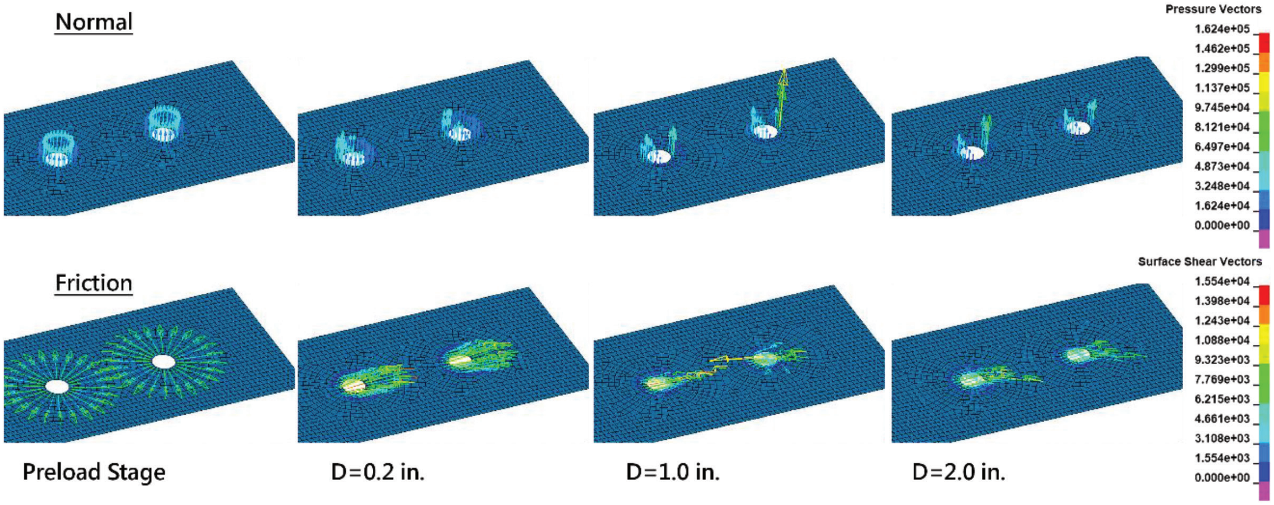

Fig. 36. Normal and friction stresses on the surface of the splice plate (Model 3).

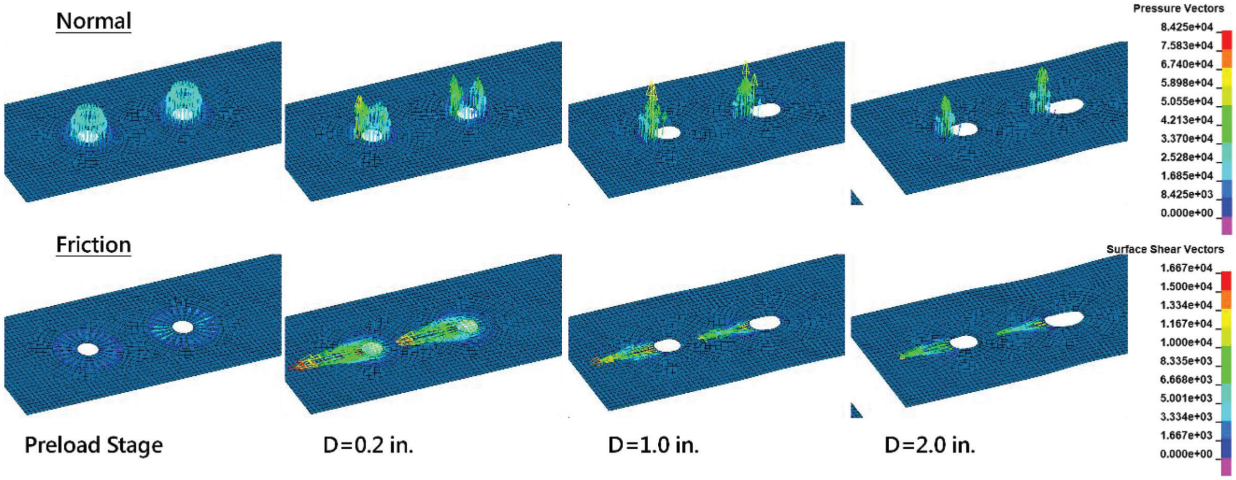

Fig. 37. Normal and friction stresses on the surface of the faceplate (Model 3).

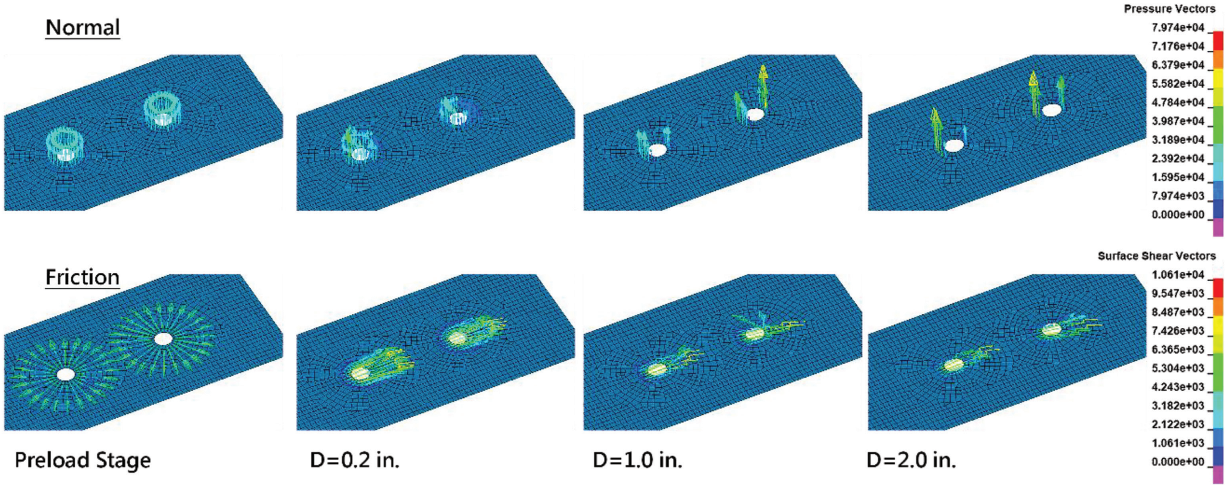

Fig. 38. Normal and friction stresses on the surface of the splice plate (Model 4).

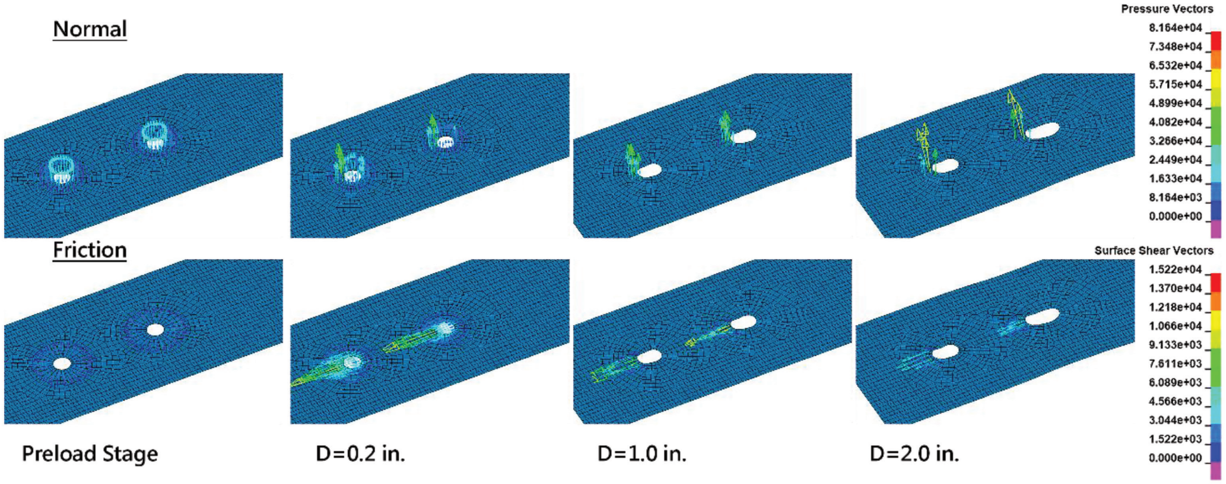

Fig. 39. Normal and friction stresses on the surface of the faceplate (Model 4).

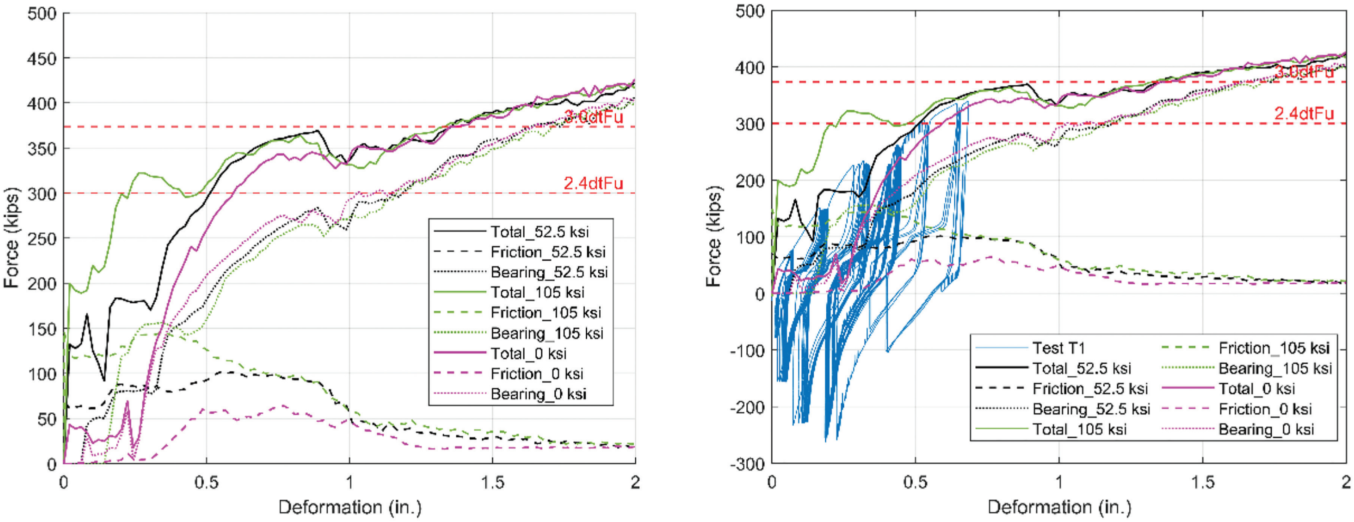

(a) FEM analysis results *(b) FEM analysis vs. test*

Fig. 40. Force-deformation curve of Model T1 with different pretensions.

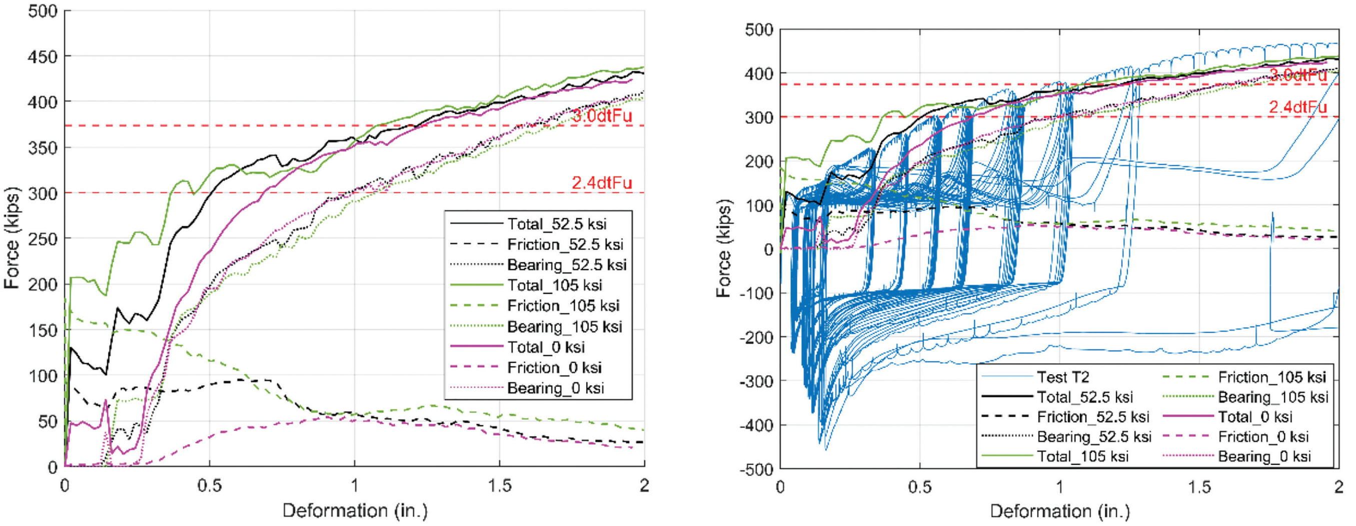

(a) FEM analysis results *(b) FEM analysis vs. test*

Fig. 41. Force-deformation curve of Model T2 with different pretensions.

was 1,126 kips, reached at −0.2 in. deformation. For comparison, the nominal axial strength of the connection can be calculated as:

$$P_{T,n} = A_s F_y + 0.85 A_c f_c' \\ = -1{,}194 \text{ kips} \tag{5}$$

where the compressive strength of concrete, f_c', is equal to 5.5 ksi. The peak strength reached by the numerical model is less than this value because the strength of the steel splice is governed by bearing, which developed at stresses over the plate cross section, A_s, of less than F_y. For comparison, at peak total strength in the numerical model, the average stress developed in the steel and concrete area was –17.5 ksi and –6.32 ksi, respectively. At that deformation level, bolts are bearing on the bolt holes but have not produced large hole deformations yet, as shown in Figure 47.

To investigate the load-transfer mechanisms that develop in the splice region, Figures 48 and 49 provide global and local free-body diagrams of the forces between steel plates and between steel and concrete there. All force components shown in the free-body diagrams are plotted in Figures 50 and 51. The force equilibrium formulas are presented below, and Figure 52 shows the results of these formulas, confirming compliance with force equilibrium.

$$sumG1 = P_{FP} - F_{r5} + F_6 - P_{SP1} - P_{SP2} \tag{6}$$

$$sumG2 = P_{FP} + F_{r1} + F_{r4} - F_{r5} - \\ B_1 + B_2 + B_3 - P_{SP1} - P_{SP2} \tag{7}$$

$$sumL1 = F_{r1} + F_{r4} + B_2 - P_{SP1} \tag{8}$$

$$sumL2 = P_{FP} - B_1 - F_{r2} - F_{r3} \tag{9}$$

$$sumL3 = F_{r3} + F_{r4} - F_{r5} + P_{FP} + B_3 - P_{SP2} \tag{10}$$

At the initial stage (before connection slip and at −0.01 in. deformation), the axial forces P_{FP}, P_{SP1}, and P_{SP2} were 46.2, 27.6, and 22.0 kips, respectively. At this stage, the friction forces F_{r2} and F_{r3}, each contributing 23.1 kips, reached their slip-critical state. Meanwhile, the friction forces F_{r1} and F_{r4} were −0.9 and 4.2 kips, respectively. After the connection slip, the axial forces P_{FP} and P_{SP1}, and the friction forces F_{r2} and F_{r3} remained unchanged as they were in plateau. However, the axial force P_{SP2} and friction force F_{r4} kept increasing and plateaued at 42.7 and 20.0 kips at a deformation of −0.05 in. At this point, the contact force F_6 acting on the nuts reached 17 kips.

It can be observed that the bearing force B_1 initiated at a deformation of −0.12 in. and continued to increase until it plateaued at 45 kips at −0.17 in. deformation. During this period, the axial force P_{FP} increased to 87 kips, and the axial force P_{SP1} rose to 42 kips, approaching the magnitude of P_{SP2}. Concurrently, the friction force F_{r1} changed from –3.3 to 20.7 kips, reaching its plateau at deformation of –0.17 in. Furthermore, the contact force F_6 changed from 11.3 to –2 kips. At a deformation of −0.23 in., the bearing forces acting on splice plates (B_2 and B_3) began to develop.

In other words, the sequence of events can be described as follows: When the axial load on the faceplate, P_{FP}, increased to the slip-critical resistance of bolts at a deformation of –0.01 in., the sliding intended to occur on the friction forces between faceplate and splice plate (F_{r2} and F_{r3}). However, the sliding was prevented because the nuts embedded inside concrete could not move. Between deformation of –0.01 to –0.05 in., the friction force between the bolt nut and inside splice plate, F_{r4}, the contact force between the bolt nut and concrete, F$_6$, and the axial force on the inside splice plate, P_{SP2}, continued to increase to a

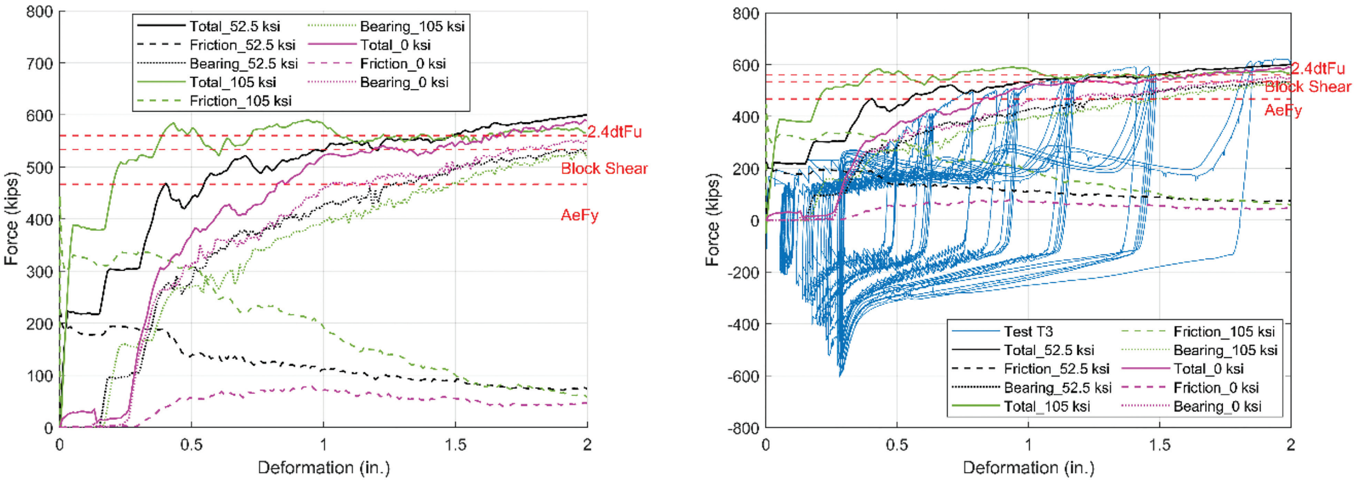

(a) FEM analysis results   *(b) FEM analysis vs. test*

Fig. 42. Force-deformation curve of Model T3 with different pretensions.

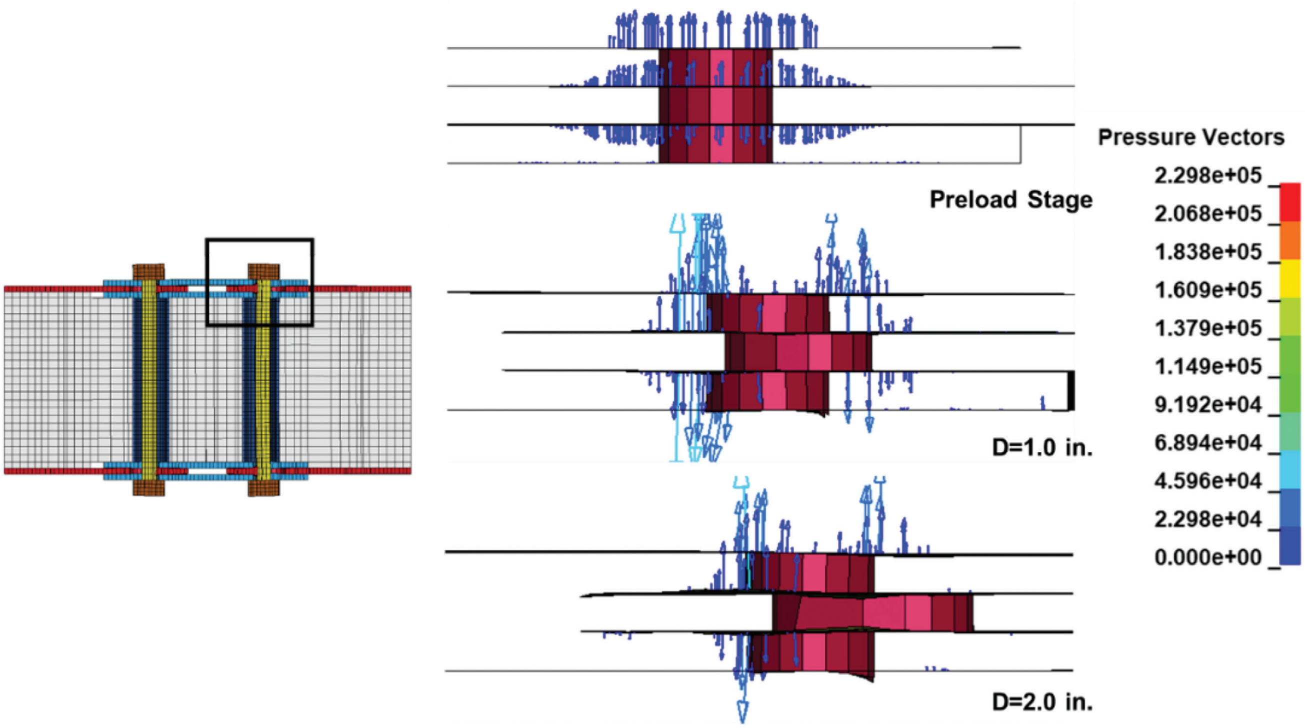

Fig. 43. Clamping stress vectors in Model T2.

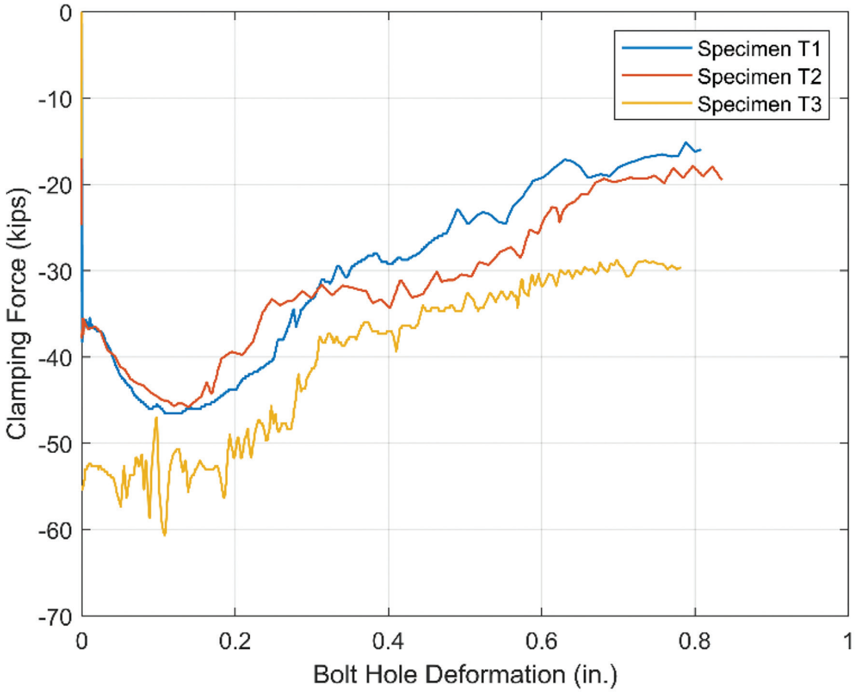

Fig. 44. Clamping force-hole deformation curve of Models T1–T3.

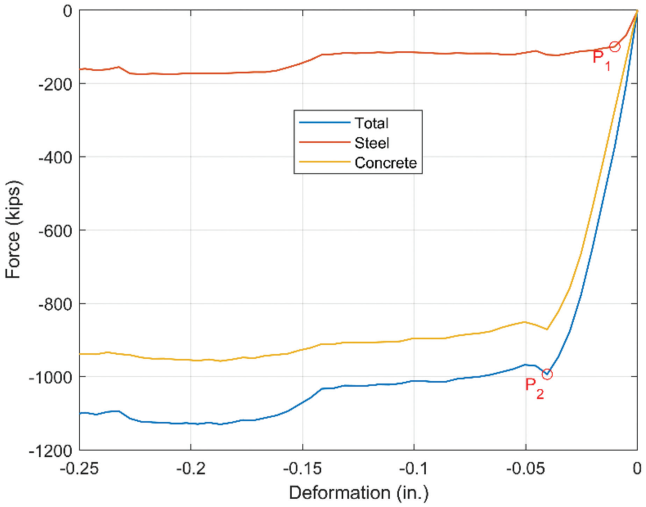

Fig. 45. Force-deformation curve of Model T1 in compression.

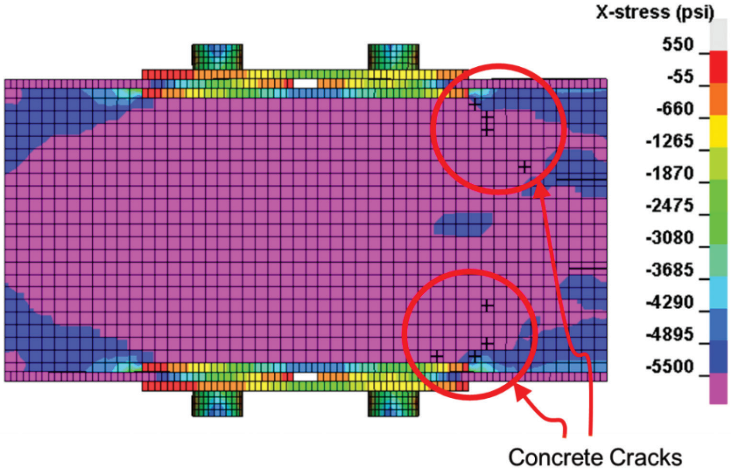

Fig. 46. Initiation of concrete cracks of Model T1 in compression.

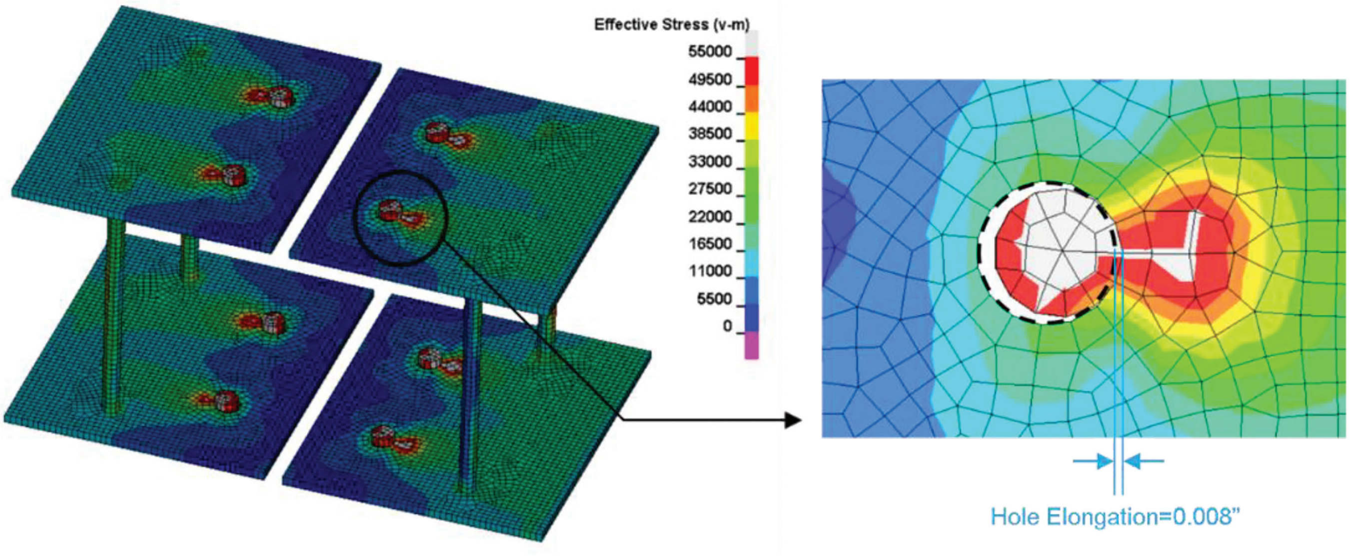

Fig. 47. Bolt hole elongation at −0.20 in. deformation.

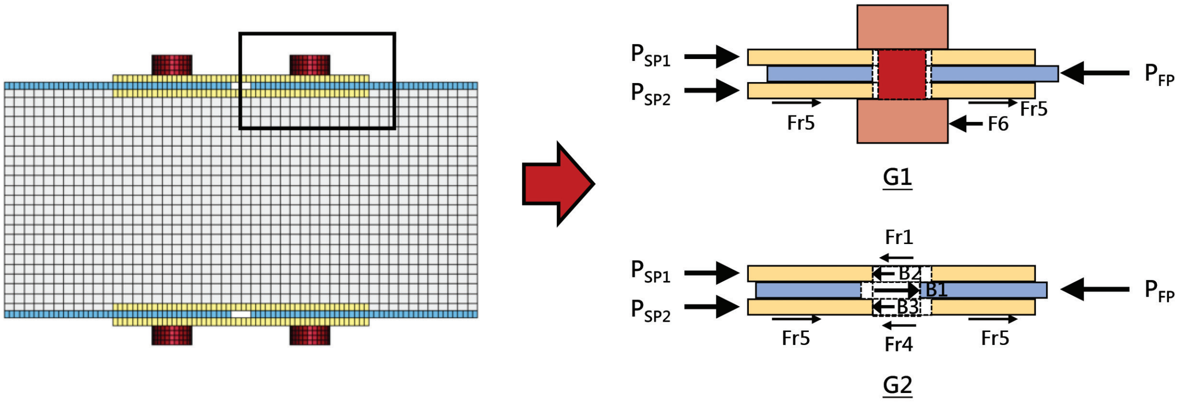

Fig. 48. Global free-body diagram of Model T1.

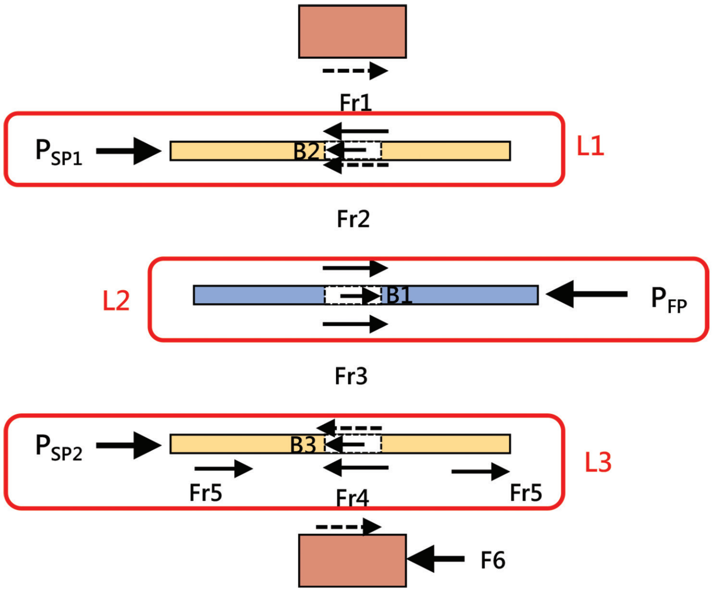

Fig. 49. Local free-body diagram of Model T1.

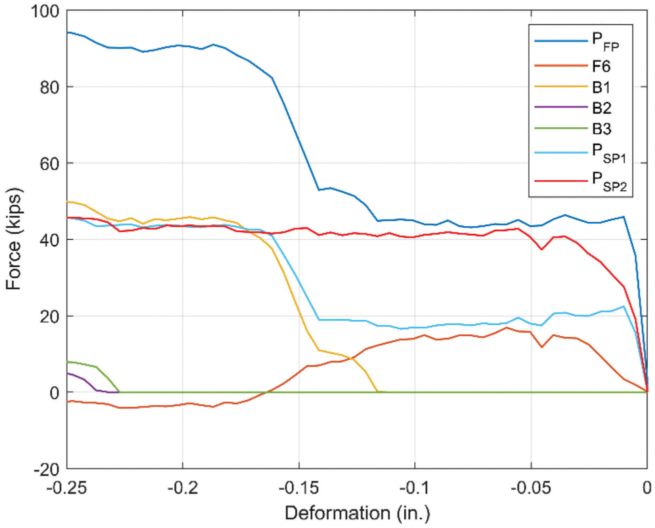

Fig. 50. Axial forces on steel plates and bearing forces in Model T1.

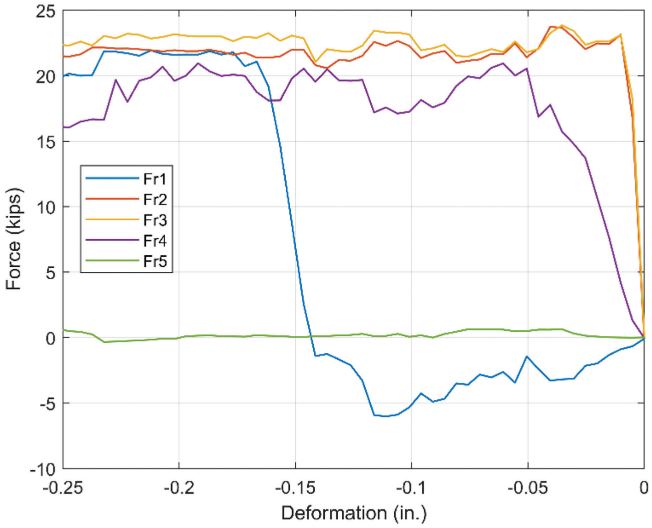

Fig. 51. Friction forces in Model T1.

plateau at a deformation of −0.05 in. After the bolt shank started touching bolt holes at a deformation of −0.12 in., the axial forces on the faceplate and splice plate, P_{FP} and P_{SP1}, bearing force on the faceplate, B_1, and friction force between the bolt head and the outside splice plate, F_{r1}, started to develop. These forces increased to a plateau until the bearing force on the faceplate, B_1, reached its plateau at a deformation of −0.17 in. Finally, at −0.23 in. deformation, the axial forces on the faceplate, P_{FP}, and the axial forces on the splice plates, P_{SP1} and P_{SP2}, increased again as the bearing forces splice plates, B_2 and B_3, started to develop.

During the preceding compressive deformation, the friction forces did not experience a significant reduction compared to the connection subjected to tension because the hole elongations are limited due to the presence of the concrete.

SUMMARY AND CONCLUSIONS

This study explored the effect of bolt pretension on bearing strength in bolted connections of all-steel and C-PSW/CF models through finite element analysis. Finite element models and simplified free-body diagrams with contact springs were used to examine the relationship of the clamping and bearing stress development in bolted connections. For connections under tension, friction forces generally decrease as the bolt hole elongation increases due to combined effects of the inelastic deformation and bending of bolt shanks, loss of contact area and stiffness in the initial contact springs, and thinning of the faceplates in tension due to Poisson's effect. These factors significantly impact the development of friction, indicating that for design, the bearing strength and slip-resistance strengths cannot be combined to calculate the overall strength of a bolted connection. In a bolted C-PSW/CF connection subjected to compression, the elongation of bolt holes due to bearing forces is restricted. Initially, the friction force reaches its slip-critical resistance, after which the axial force is transferred to the concrete. As the concrete reaches its compressive strength and begins to crack, its contribution diminishes, leading to the development of slip in the steel connection. The friction forces remain at a plateau before significant slip deformation occurs. While the creep effect of concrete is beyond the scope of this study, it is not anticipated to have a significant effect other than possibly slightly delaying the transfer of axial force to concrete once the friction force reaches its slip-critical resistance. Creep should not impact pretension when the material within the grip of the bolts is all steel, but it is unknown whether it could lead to a loss of pretension for the case of through rods with pipe-sleeves. This does not affect the conclusions of this study but may be investigated in future research.

ACKNOWLEDGMENTS

This research was supported by the Charles Pankow Foundation (CPF), the American Institute of Steel Construction (AISC), the MKA Foundation, and Atlas Tube/Zekelman through CPF research grant 02-21. All opinions, findings, conclusions, and recommendations presented in this paper are those of the authors and do not necessarily reflect the view of the sponsors. The researchers are also grateful

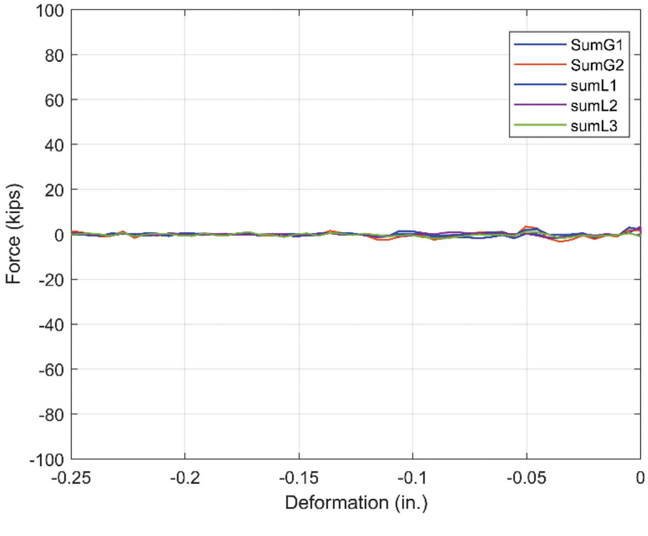

Fig. 52. Force equilibrium of Model T1.

for the technical guidance of its Project Advisory Group members (Glenn Bell, National Institute of Standards and Technology; Ron Klemencic, Chair and CEO, Magnusson Klemencic and Associates; Jim Malley, Senior Principal with Degenkolb Engineers; Rafael Sabelli, Principal and Director of Seismic Design, Walter P. Moore; Devin Huber, Director of Research at AISC; and Christopher Raebel and Larry Kruth, current and former Vice Presidents at AISC).

REFERENCES

Agrawal, S. (2020), "Seismic Design Coefficients for Composite Plate Shear Walls—Concrete Filled (C-PSW/CF)," Purdue University, West Lafayette, Ind.

AISC (2022a), *Seismic Provisions for Structural Steel Buildings*, ANSI/AISC 341-22, American Institute of Steel Construction, Chicago, Ill.

AISC (2022b), *Specification for Structural Steel Buildings*, ANSI/AISC 360-22, American Institute of Steel Construction, Chicago, Ill.

Alzeni, Y. (2014), "Cyclic Inelastic Behavior of Concrete Filled Sandwich Panel Walls Subjected to In-Plane Flexure," State University of New York at Buffalo, Buffalo, N.Y.

Alzeni, Y. and Bruneau, M. (2017), "In-Plane Cyclic Testing of Concrete-Filled Sandwich Steel Panel Walls with and without Boundary Elements," *Journal of Structural Engineering*, Vol. 143, No. 9. https://doi.org/10.1061/(asce)st.1943-541x.0001791

ASCE (2022), *Minimum Design Loads and Associated Criteria for Buildings and Other Structures*, ASCE/SEI 7-22, American Society of Civil Engineers, Reston, Va.

Back, J.D. and Bouwman, L.P. (1959), "The Friction Factor under Influence of Different Tightening Methods of the Bolts and of Different Conditions of the Contact Surfaces," Report 6-59-9-VB-3, Stevin Laboratory, Delft University of Technology, Delft, the Netherlands.

Brown, J.D., Lubitz, D.J., Cekov, Y.C., Frank, K.H., and Keating, P.B. (2007), "Evaluation of Influence of Hole Making upon the Performance of Structural Steel Plates and Connections," Report No. FHWA/TX-07/0-4624-1, University of Texas at Austin, Austin, Tex.

Franceschetti, N. and Denavit, M.D. (2021), "Tearout Strength of Concentrically Loaded Bolted Connections," *Engineering Journal*, AISC, Vol. 58, No. 3. https://doi.org/http://dx.doi.org/10.62913/engj.v58i3.1180

Frank, K.H. and Yura, J.A. (1981), "An Experimental Study of Bolted Shear Connections," Report DOT-FH-11-8900, Federal Highway Administration, Washington, D.C.

Hallquist, J.O. (2006), *LS-DYNA® Theory Manual*, Livermore Software Technology Corporation (LSTC), Livermore, Calif.

Hirano, M. (1970), "Bearing Stresses in Bolted Joints," Society of Steel Construction of Japan, Vol. 6, No. 58.

Jones, J. (1958), "Bearing-Ratio Effect on Strength of Riveted Joints," *Transactions ASCE*, Vol. 123, pp. 964–972.

Kim, H.J. and Yura, J.A. (1996), "The Effect of End Distance on the Bearing Strength of Bolted Connections," University of Texas at Austin, Austin, Tex.

Kizilarslan, E. (2021), "Experimental and Analytical Inelastic Behavior of C- and T-Shaped Composite Plate Shear Walls/Concrete-Filled (C-PSW/CF)," State University of New York at Buffalo, Buffalo, N.Y.

Kizilarslan, E. and Bruneau, M. (2021), "Hysteretic Behavior of Repaired C-Shaped Concrete Filled-Composite Plate Shear Walls (C-PSW/CF)," *Engineering Structures*, Vol. 241. https://doi.org/10.1016/j.engstruct.2021.112410

Kizilarslan, E. and Bruneau, M. (2023), "Cyclic Behavior of T-Shaped Composite Plate Shear Walls–Concrete Filled," *Journal of Structural Engineering*, Vol. 149, No. 8. https://doi.org/10.1061/jsendh.Steng-11693

Kulak, G.L., Fisher, J.W., and Struik, J.H.A. (1987), "Guide to Design Criteria for Bolted and Riveted Joints," RCSC, Chicago, Ill.

Lewis, B.E. and Zwememan, F.J. (1996), "Edge Distance, Spacing, and Bearing in Bolted Connections," Oklahoma State University, Stillwater, OK.

Liu, J.-H. and Bruneau, M. (2024), "Cyclic Tension Behavior of Concrete Filled Composite Plate Shear Wall Components having Bolted Splices" (under review), *Engineering Structures*.

Može, P. (2018), "Bearing Strength at Bolt Holes in Connections with Large End Distance and Bolt Pitch," *Journal of Constructional Steel Research*, Vol. 147, pp. 132–144. https://doi.org/10.1016/j.jcsr.2018.04.006

Nunse, W.H. (1959), "The Effect of Bearing Pressure on the Static Strength of Riveted Connections," *Bulletin 454*, Engineering Experiment Station, University of Illinois, Urbana, Ill.

Polat, E. and Bruneau, M. (2018), "Cyclic Inelastic In-Plane Flexural Behavior of Concrete-Filled Sandwich Steel Panel Walls," *Engineering Journal*, AISC, Vol. 55, No. 1, pp. 45–76.

Sener, K.C. and Varma, A.H. (2014), "Steel-Plate Composite Walls: Experimental Database and Design for Out-of-Plane Shear," *Journal of Constructional Steel Research*, Vol. 100, pp. 197–210. https://doi.org/10.1016/j.jcsr.2014.04.014

Shafaei, S., Varma, A.H., Seo, J., and Klemencic, R. (2021), "Cyclic Lateral Loading Behavior of Composite Plate Shear Walls/Concrete Filled," *Journal of Structural Engineering*, Vol. 147, No. 10. https://doi.org/10.1061/(asce)st.1943-541x.0003091

Varma, A.H., Malushte, S.R., Sener, K., and Lai, Z. (2014), "Steel-Plate Composite (SC) Walls for Safety Related Nuclear Facilities: Design for In-Plane and Out-of-Plane Demands," *Nuclear Engineering and Design*, Vol. 269, pp. 240–249.